UNIVERSITY OF CALIFORNIA SAN DIEGO

A Study of Conversion Reactions for Nanomaterial Synthesis and Energy Storage Applications

A Dissertation submitted in partial satisfaction of the requirements
for the degree Doctor of Philosophy

in

Materials Science and Engineering

by

Victoria Petrova

Committee in charge:

Professor Ping Liu, Chair
Professor Renkun Chen
Professor Zheng Chen
Professor Alina Schimpf
Professor Oscar Vazquez

2023

The Dissertation of Victoria Petrova is approved, and it is acceptable in quality and form for publication on microfilm and electronically.

University of California San Diego

2023

DEDICATION

I would like to dedicate this thesis to my parents who have unwaveringly supported me through everything and taught me the importance of persistence and caring for others (and a good cup of tea).

And to my partner Tom who never fails to make me laugh and always believes I can tackle the bigger waves.

TABLE OF CONTENTS

LIST OF FIGURES

LIST OF TABLES

LIST OF ABBREVIATIONS

AC impedance	Alternating current impedance
NW	Nanowires
SEM	Scanning electron microscopy
TEM	Transmission electron microscopy
XRD	X-ray diffraction
GITT	Galvanostatic intermittent titration technique
JMAK	Johnson, Mehl, Avrami, Kolmogorov

ACKNOWLEDGEMENTS

I would like to thank Professor Liu for his support and patient guidance while I figured out how research works. I am also grateful to the members of the Liu Group; my experience would not have been the same had it not been for so many people willing to help and share insights and being amazing team-mates.

Additionally, my collaboration with Adam Corrao in the Khalifah group broadened my perspective on what it means to do good, detailed materials science and the persistence required to fully understand complex data. Adam was the driving force behind every beamtime and his guidance in analyzing synchrotron data was unparalleled.

Outside of the lab, I would like to acknowledge the impact of the friends I have made through volleyball, rock climbing and acro. When one too many experiments did not turn out how I expected, they were there to lift me up and remind me to take time to play and do some handstands.

Chapter 2, in part is currently being prepared for submission for publication of the material, V. Petrova**,** E. Maria, J. Ferrari, G. Kamm, J. Neilson, K. Thornton, K. Chapman, P. Liu. The dissertation author was the primary researcher and author of this material.

Chapter 3, in full, is a reprint of the material as it appears in RSC Advances, V. Petrova, A. A. Corrao, S. Wang, Y. Xiao, K. W. Chapman, E. E. Fullerton, P. G. Khalifah and P. Liu. 2022. The dissertation author was the primary researcher and author of this paper.

Chapter 4, in part is currently being prepared for submission for publication of the material, V. Petrova, J. Zhou, S. Wang, P. Liu. The dissertation author was the primary researcher and author of this material.

VITA

2017 Bachelor of Science in Materials Science and Engineering, Massachusetts Institute of Technology

2018 Master of Science in Materials Science and Engineering, University of California San Diego

2023 Doctor of Philosophy in Materials Science and Engineering, University of California San Diego

PUBLICATIONS IN PROGRESS

1. **V. Petrova,** E. Maria, J. Ferrari, G. Kamm, J. Neilson, K. Thornton, K. Chapman, P. Liu. (2023) Tracking progression of solid-state metathesis reaction with AC Impedance

2. **V. Petrova**, J. Zhou, S. Wang, P. Liu. (2023) Exploring kinetics behind FeCl3 and FeF3 conversion reactions in all solid-state batteries

PUBLICATIONS

1. A. A Corrao, G. S Mattei, C. M Coaty, Z. Li, **V. Petrova**, L. Yin, P. Liu, P. G Khalifah. (2023) Salt-Mediated Coarsening in Conversion-Reaction-Synthesized Nanoporous Metals and Nanocomposites Resolved through In Situ Synchrotron Diffraction Studies, *Chemistry of Materials*

2. **V. Petrova**, A. A. Corrao, S. Wang, Y. Xiao, K. W. Chapman, E. E. Fullerton, P. G. Khalifah and P. Liu. (2022) Synthesis of flexible Co nanowires from bulk precursors, *RSC Advances*

3. R. D. McAuliffe, G. Huang, D. Montiel, A. Mehtan, R. C. Davis, **V. Petrova**, K. L. Browning, J. R. Neilson, P. Liu, K. Thornton and G. M. Veith. (2022) Thin-Film Paradigm to Probe Interfacial Diffusion during Solid-State Metathesis Reactions, *Advanced Energy Materials*

4. S. Feng, **V. Petrova**, A. A Corrao, S. Wang, K. Yang, P. G Khalifah, P. Liu. (2022) Morphological Control of Nanoporous Copper Formed from Conversion Reaction Synthesis, *The Journal of Physical Chemistry C*

5. R. D. McAuliffe, **V. Petrova**, M. J. McDermott, J. L. Tyler, E. C. Self, K.A. Persson, P. Liu, and G. M. Veith. (2021) Synthesis of model sodium sulfide films, *Journal of Vacuum Science & Technology A*

6. C. M. Coaty, A. Corrao, **V. Petrova***, T. Kim, D. P. Fenning, P. Khalifah, P. Liu (2021) Anisotropic Nanoporous Morphology of ZnO-Supported Co that Enhances Catalytic Activity, *Nanoscale* ***Co-first author**

7. Z. Zheng, H. Wu, H. Liu, Q. Zhang, X. He, S. Yu, **V. Petrova**, J. Feng, R. Kostecki, P. Liu, D. Peng, M. Liu, and M. S. Wang (2020) Achieving Fast and Durable Lithium Storage through Amorphous FeP Nanoparticles Encapsulated in Ultrathin 3D P-Doped Porous Carbon Nanosheets, *ACS Nano*

8. Q. Chen, Y. Cheng, H. Liu, Q. Zhang, **V. Petrova**, H. Chen, P. Liu, D. Peng, M. Liu, and M. S. Wang. (2020) Hierarchical Design of Mn2P Nanoparticles Embedded in N, P-Co-doped Porous Carbon Nanosheets Enables Highly Durable Lithium Storage, *ACS Applied Material Interfaces*

9. M. S. Gonzalez, Q. Yan, J. Holoubek, Z. Wu, H. Zhou, N. Patterson, **V. Petrova**, H. Liu, and P. Liu. (2020) Draining Over Blocking: Nano-Composite Janus Separators for Mitigating Internal Shorting of Lithium Batteries, *Advanced Materials*

10. C. M. Coaty, A. A. Corrao, **V. Petrova**, P. G. Khalifah, P. Liu (2019) Morphological Tuning of Nanoporous Metals Prepared with Conversion Reaction Synthesis via Thermal Annealing, *Journal of Physical Chemistry C*

11. X. Xing, Y. Li, X. Wan, **V. Petrova**, H. Liu, and P. Liu (2019) Cathode electrolyte interface enabling stable Li-S batteries, *Energy Storage Materials*

12. B. Lee, S. Cui, X. Xing, H. Liu, X. Yue, **V. Petrova**, H. Lim, R. Chen, and P. Liu (2018) Dendrite Suppression Membranes for Rechargeable Zinc Batteries, *ACS Appl. Mater. Interfaces*.

13. H. Liu, X. Yue, X. Xing, Q. Yan, J. Huang, **V. Petrova**, H. Zhou, P. Liu (2018) A Scalable 3D Lithium Metal Anode, *Energy Storage Materials*

14. B. Lee, Z. Wu, **V. Petrova**, X. Xing, H. Lim, H. Liu, and P. Liu (2018) Analysis of rate-limiting factors in thick electrodes for electric vehicle applications, *J. Electrochemical Society*

ABSTRACT OF THE DISSERTATION

A Study of Conversion Reactions for Nanomaterial Synthesis and Energy Storage Applications

by

Victoria Petrova

Doctor of Philosophy in Materials Science and Engineering

University of California San Diego, 2023

Professor Ping Liu, Chair

A great challenge in solid-state synthesis is the ability to predict and design reaction pathways to synthesize new materials. In order to rationally plan synthesis procedures, one must understand the reaction mechanism involving thermodynamic and kinetic forces such as

diffusion, interfacial reactions, activation energies and metastable states. This work focuses on studying conversion reactions as a platform to investigate solid-state reaction kinetics, nanomaterial synthesis and energy storage applications. Conversion reactions are essentially displacement reactions in which the cations of two ionic compounds are exchanged to form a two-phase nanocomposite. They may be used for scaling synthesis procedures by lowering the activation energy of a reaction and can also serve as high-capacity battery materials due to the multiple electron transfers that occur per redox center.

This work involves three parts: 1) developing an in-situ method of tracking a solid-state conversion reaction using AC impedance, 2) applying a conversion reaction to synthesize 1D nanomaterials from bulk precursors and 3) exploring the kinetics behind conversion reactions in all solid-state batteries. The first part leverages the sensitivity of AC impedance to be used as a characterization technique to help detect the onset of a reaction by measuring conductivity and using the data to provide insights into the kinetics of the reaction. The second and third parts apply conversion reactions to help tune nanomaterial synthesis and compare reaction mechanisms of iron halide conversion batteries.

CHAPTER 1: INTRODUCTION TO CONVERSION REACTIONS AND THEIR APPLICATIONS

This work focuses on studying conversion reactions as a platform to investigate solid-state reaction kinetics, nanomaterial synthesis and energy storage applications. Conversion reactions are essentially displacement reactions in which the cations of two ionic compounds are exchanged to form a two-phase nanocomposite. They may be used for scaling synthesis procedures by lowering the activation energy of a reaction and can also serve as high-capacity battery materials due to the multiple electron transfers that occur per redox center. This work involves three parts: 1) developing an in-situ method of tracking a solid-state conversion reaction using AC impedance, 2) applying a conversion reaction to synthesize 1D nanomaterials from bulk precursors and 3) exploring the kinetics behind conversion reactions in all solid-state batteries.

The first section focuses on using AC impedance as an in-situ characterization technique to study solid-state reactions. In particular, the formation of pyrite, FeS_2, through the metathesis reaction, $Na_2S_2 + FeCl_2 \rightarrow NaCl + FeS_2$ is used as a case study since all the reactants and products except for FeS_2 are highly resistive, therefore the conductivity of the system can be used as an approximation for the formation of conducting FeS_2 species and serve as a marker for reaction progress. AC impedance is sensitive to changes in phase, homogeneity, morphology and volume fraction down to the nanometer length scale allowing us to probe the onset of reactions and gain insight into the kinetics governing the reaction. By measuring the impedance while the system is heated isothermally at different temperatures, new insights into the kinetics and potential energy barriers as well as metastable states during the reaction can be analyzed. This work focuses on the effect of particle size of the precursors and how different combinations of large and small precursors may affect the reaction pathway. In particular, we hypothesize that small $FeCl_2$ should

have a large effect if the reaction becomes diffusion-limited by accommodating Fe's low mobility with smaller transport paths. Isothermal experiments show that there is a plateau in conductivity after ~1 hr of heating reflecting a potential two-step reaction in which there is an activation energy barrier to form certain intermediates before forming the final product. Interestingly, the combination of small $FeCl_2$ and large Na_2S_2 passes this plateau showing a different reaction pathway enabled by smaller transport distances for Fe and fast diffusion through Na_2S_2. Nucleation and growth models can be fit to the later stages of the reaction to show it becomes diffusion-limited. XRD can corroborate the conductivity data at higher temperatures and longer time periods when there is a significant enough formation of products to detect changes in phase fraction and evolution.

The second aspect of this work applies conversion reactions to tune nanomaterial morphology. We are able to synthesize 1D Co nanowires from a previously established procedure of making nanoporous metals by changing the dilution of the precursor and using an anisotropic crystal structure (hcp instead of ccp). It is incredibly rare to be able to produce 1D nanomaterials without the use of external stimuli such as templates or ligands due to the thermodynamic stability and preference for materials to minimize their free surface energy. Synchrotron XRD is used to determine the crystal structure of the nanowires, showing it is a mixture of hcp and ccp. SEM and TEM are used to characterize the physical properties of the nanowires and comparisons across similar systems are used to deduce the formation mechanism of what drives the 1D growth.

Lastly, $FeCl_3$ and FeF_3 cathode materials are studied to better understand the hysteresis commonly found in conversion cathode materials. FeF_3 has been extensively researched due to its promise of high capacity as each redox center accommodates 3 Li ions. However, $FeCl_3$ has not been studied yet due to dissolution issues in the electrolyte. Recent progress in solid state halide

electrolytes have allowed us to study $FeCl_3$ in solid-state batteries. The goal of the work is to compare the effect of the anion, Cl vs F, based on the idea that there are different surface energies between the products formed during lithiation which can affect path hysteresis and potentially reveal a new reaction worthy of further study. LiCl shows lower diffusion barriers for adatoms than LiF which may significantly encourage Li diffusion and aid the conversion reaction to fully form LiCl and Fe. We expect this would result in lower hysteresis during cycling. Indeed, analyzing the second cycle data and comparing the voltage relaxation values from GITT measurements indicate $FeCl_3$ undergoes significantly less hysteresis, especially during the conversion reaction of the second voltage plateau. EIS also reveals further insights into the evolution of the impedance of the cell throughout cycling.

CHAPTER 2: TRACKING PROGRESSION OF SOLID-STATE METATHESIS REACTION WITH AC IMPEDANCE

2.1 Introduction

Solid state synthesis is essential in producing materials to meet technological demands. However, our ability to predict and design reaction pathways to synthesize new materials is still limited.[1,2] Determining the reaction mechanism involving thermodynamic and kinetic forces such as diffusion, interfacial reactions, activation energies and metastable states is a great challenge impeding the design and prediction of new synthesis routes.[3] The general approach to rational synthesis planning is an iterative process of hypothesis, synthesis, characterization, testing and repetition ad nauseum.[1] To control and efficiently use chemical synthesis methods, one needs to know the reaction processes.[4]

The main difficulty in using a suitable in-situ characterization technique to study solid-state reactions lies in finding a technique adaptable for the time lengths (seconds to hours), length scales (nanometers to microns), and experiment conditions (temperature, pressure, gas flow, etc.) of the system being studied.

While many characterization techniques have been developed to probe composition, structure, morphology and other ex-situ properties, in-situ methods need to be utilized in order to understand reaction mechanisms as they occur, often-times in harsh and varied operating conditions. In-situ characterization techniques in thermal, spectroscopy, diffraction and computation areas help make the iterative synthesis process more efficient and elucidate reaction pathways and metastable phases. The most common technique for studying in-situ reactions is synchrotron XRD.[5–8] Thermogravimetric studies involve the use of TGA to study scenarios such as the decomposition and activation of dawsonite-type compounds to oxide catalysts.[9] In-situ solid-state NMR has been applied to study fluorination of y-Al_2O_3,[6] as well as silicate formation

at high temperatures.[10] An emerging technique is in-situ TEM which has been used to probe the interface of the solid-state reaction between aluminum and germanium nanowires during heating.[11] Additionally, computation methods based on fundamental energy landscapes and materials properties databases have provided strides in the more proactive synthesis-by-design approach. Persson et al have developed a reaction network model based on thermodynamic phase diagrams and kinetics to predict and experimentally synthesize the solid-state compounds $YMnO_3$, $Y_2Mn_2O_7$, Fe_2SiS_4, and $YBa_2Cu_3O_6$.[12]

In this work, AC Impedance is used to probe the onset of reactions and give insight into the kinetics governing the reaction. While electrochemical impedance spectroscopy is widely used to investigate reaction and transport processes in electrochemical systems, its use as an in-situ characterization technique for solid-state reactions has only been realized in a few use cases for studying corrosion mechanisms.[13,14] EIS has many advantages and can be a powerful tool especially when coupled with other complementary in-situ techniques. By comparing the input of an alternating potential with the output current and potential, it can evaluate kinetics and mass transport, determine diffusion coefficients and rate constants and provide insights into interfacial reactions at the surface of particles.[15] EIS is therefore sensitive to changes in phase, homogeneity, morphology and volume fraction down to the nanometer length scale.[16] Additionally, it is an accessible lab-scale technique that takes around one to five minutes per measurement.

This work focuses on monitoring the formation of pyrite, FeS_2, through the metathesis reaction, $Na_2S_2 + FeCl_2 \rightarrow NaCl + FeS_2$. FeS_2 initially gained interest for its use in photovoltaics due to its high optical absorption coefficient and suitable band gap, however it is now also growing popular in rechargeable batteries because of its high conductivity and capacity. Additionally, FeS_2 is valued for its earth abundance, nontoxicity and low fabrication costs.[17–19] This

metathesis reaction is used as a case study since all the reactants and products except for FeS_2 are highly resistive, therefore the conductivity of the system can be used as an approximation for the formation of conducting FeS_2 species and serve as a marker for reaction progress. By measuring the impedance while the system is heated isothermally at different temperatures, new insights into the kinetics and potential energy barriers as well as metastable states during the reaction can be analyzed (Figure 1). During initial phase of the reaction, the formation of the conductive products occurs at the interfaces. The formation of a percolating network manifests as a rapid rise in conductivity. Further increase in conductivity can be used as a proxy for volumetric increase of the conducting phase assuming an isotropical structure. Intuitively, conductivity of the reaction mixture is also a function of microstructure in addition to compositions.

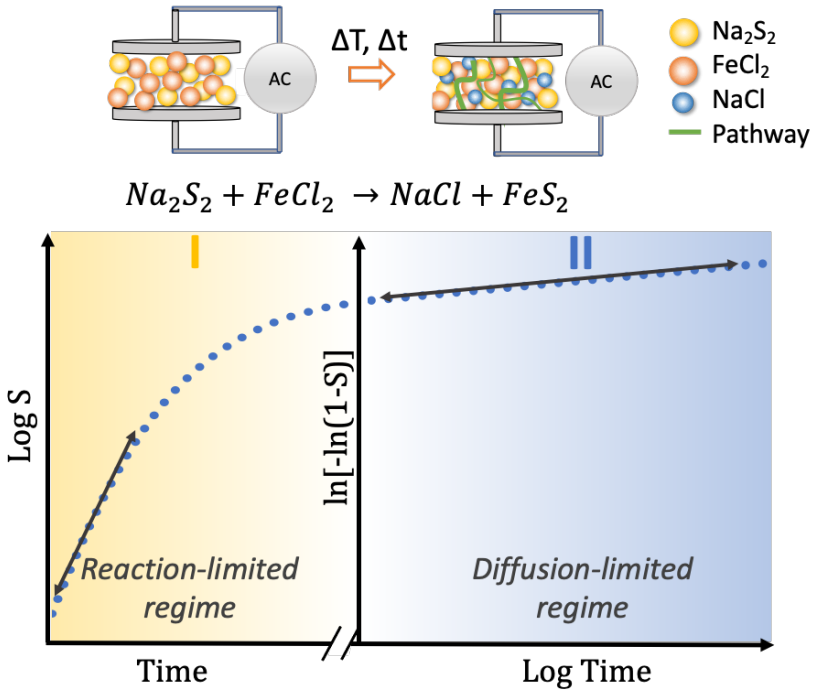

Figure 2.1: Schematic of conductivity trends with time during isothermal heating showing the progression from reaction-limited to diffusion-limited regimes.

The general consensus in how solid-state reactions progress involves a nucleation and growth step followed by diffusion for subsequent reaction completion.[23–25] Phase transformation models have largely been developed by building on the JMAK theory through addressing specific use cases and discussion of the Avrami exponent,[26–28] however most models are derived theoretically. Experimental data used to prove the models are usually obtained through thermogravimetric and/or XRD measurements, however these techniques are not sensitive enough to detect interfacial changes.[24,29,30] Using such methods makes direct measurement of the interface and onset of reaction difficult and does not provide accurate quantitative data.

In the later stages of a reaction, diffusion tends to be the limiting factor in which particle size is known to play a role in speeding up or slowing down reaction kinetics. Reducing particle size maximizes the contact surface area, thus promoting diffusion.[19,31,32] Based on Jander's 3D diffusion model for solid state reactions, many studies have analyzed how particle size on the order of 1 to 100 um affects the nuances of the appropriate diffusion model in systems such as MgO-Al_2O_3, Fe_2O_3-V_2O_5, and $BaCO_3$-TiO_2 among others.[24,29,33,34] Beretka et al[29] determined that changing the particle size of various systems affects which model most accurately describes the reaction; for example, in the MgO-Al_2O_3 reaction, using small particles (~1-3 um) results in the best fit with a 3D diffusion model, while using large particles (~100 um) most closely resembles a first order reaction kinetics model.

2.2 Experimental Methods

Materials Synthesis: Na_2S_2 powder is synthesized from anhydrous Na_2S (Sigma-Aldrich) and elemental sulfur entirely in an argon glovebox (<0.5 ppm H_2O and <0.5 ppm O_2) to prevent air exposure. Stoichiometric amounts of anhydrous Na_2S (Sigma) and elemental sulfur are ground and mixed using an agate mortar and pestle and heated in an Al_2O_3 crucible at 230°C for 12 h.[20]

Anhydrous $FeCl_2$, 98%, is purchased from Sigma-Aldrich. Different particle sizes for both precursors are obtained through ball milling to result in small (<5 um) particles as well as hand grinding with mortar and pestle to obtain large (~100 um) particles.

Materials Characterization: Purity of Na_2S_2 is determined through X-ray diffraction using a Bruker D2 Phaser (Cu Kα radiation, λ = 1.54Å) with the sample powder sealed under Kapton tape in an argon glovebox. The main phase present is β-Na_2S_2 (P63/mmc) as well as a minor phase of Na_2S_4 (Figure S1).

For in-situ XRD measurements taken during isothermal heating, $FeCl_2$ and Na_2S_2 powders are mixed in a stoichiometric ratio and formed into a pellet in argon glovebox. Chunks of pellet material are loaded into glass capillaries (borosilicate, 1.1 mm outer diameter), sealed, assembled within a flow-cell furnace[21] and heated for 10 h at 100°C and 5 h at 245°C. During the reaction, in situ X-ray scattering data are collected using a Bruker D8 diffractometer equipped with a Mo-source beam (λ = 0.7093 Å, and 1.0 mm collimator) in a Debye-Scherrer geometry. Diffraction images are collected every 5 min using an Eiger2R_500K area detector. Two-dimensional X-ray diffraction data are then reduced to one-dimensional intensity scattering data using the Bruker DIFFRAC.EVA software.[22] Scattering data are collected for an empty glass capillary and subtracted from the time-dependent data.

Electrochemical Characterization: To measure conductivity, stoichiometric amounts of Na_2S_2 and $FeCl_2$ are mixed with varying particle sizes and pressed for two minutes before being assembled in a Swagelok cell under 30MPa of constant external pressure. The cell is then placed in an oven which is pre-heated to a predetermined temperature for isothermal experiments. The entire experiment takes place in an argon glovebox with wires connecting the cell inside the oven to a BioLogic potentiostat outside the glovebox. AC impedance spectra are taken at a frequency

of 2 MHz to 0.1 Hz at an amplitude of 0.4 V. Full spectra data is collected every three minutes. The spectra are then fitted with an RC circuit to determine the conductivities with EC-Lab software.

2.3 Results and Discussion

2.3.1 Effect of particle size

The general consensus in how solid-state reactions progress involves a nucleation and growth step followed by diffusion for subsequent reaction completion.[23–25] Phase transformation models have largely been developed by building on the JMAK theory through addressing specific use cases and discussion of the Avrami exponent,[26–28] however most models are derived theoretically. Experimental data used to prove the models are usually obtained through thermogravimetric and/or XRD measurements, however these techniques are not sensitive enough to detect interfacial changes.[24,29,30] Using such methods makes direct measurement of the interface and onset of reaction difficult and does not provide accurate quantitative data.

In the later stages of a reaction, diffusion tends to be the limiting factor in which particle size is known to play a role in speeding up or slowing down reaction kinetics. Reducing particle size maximizes the contact surface area, thus promoting diffusion.[19,31,32] Based on Jander's 3D diffusion model for solid state reactions, many studies have analyzed how particle size on the order of 1 to 100 um affects the nuances of the appropriate diffusion model in systems such as MgO-Al_2O_3, Fe_2O_3-V_2O_5, and $BaCO_3$-TiO_2 among others.[24,29,33,34] Beretka et al[29] determined that changing the particle size of various systems affects which model most accurately describes the reaction; for example, in the MgO-Al_2O_3 reaction, using small particles (~1-3 um) results in the best fit with a

3D diffusion model, while using large particles (~100 um) most closely resembles a first order reaction kinetics model.

In order to better understand the reaction mechanisms behind which FeS_2 is formed, the effect of precursor particle size is studied by comparing large and small combinations of Na_2S_2 and $FeCl_2$ to help decouple the effects of the various diffusion mobilities of each species. Literature on the mobility of Fe in during solid-state and conversion reactions show that it is notoriously slow compared to other metals.[19,35,36] Small precursors are synthesized by ball milling the powder to ~3um, whereas large precursors are sieved through a mesh sieve to isolate ~75-100um particles. A matrix of four scenarios is studied: 1) S/S - small Na_2S_2 and small $FeCl_2$, 2) B/S - big Na_2S_2 and small $FeCl_2$, 3) S/B - small Na_2S_2 and big $FeCl_2$ and 4) B/B - big Na_2S_2 and big $FeCl_2$.

Published ex-situ XRD data of the FeS_2 metathesis reaction show that FeS_2 forms at 250°C.[37] Based on this data, initial experiments studying the effect of particle size are done by measuring conductivity while the temperature is ramped from room temperature to 250°C at 1°C/min and then held for 14 hrs. These results (Figure S2) show the same trend among the four particle size scenarios of rapid increase in conductivity within the first 3hrs to saturation, then plateau for the next 14 hrs.

To investigate potentially metastable intermediate steps in the reaction, the reaction is held isothermally at temperatures ranging from 70°C to 115°C in 15C intervals (Figure 2). These temperatures are lower than the 250°C required to form FeS_2, however previous literature has shown that the NaCl product forms at ~100°C and other intermediates also play a role before the formation of FeS_2.[37]

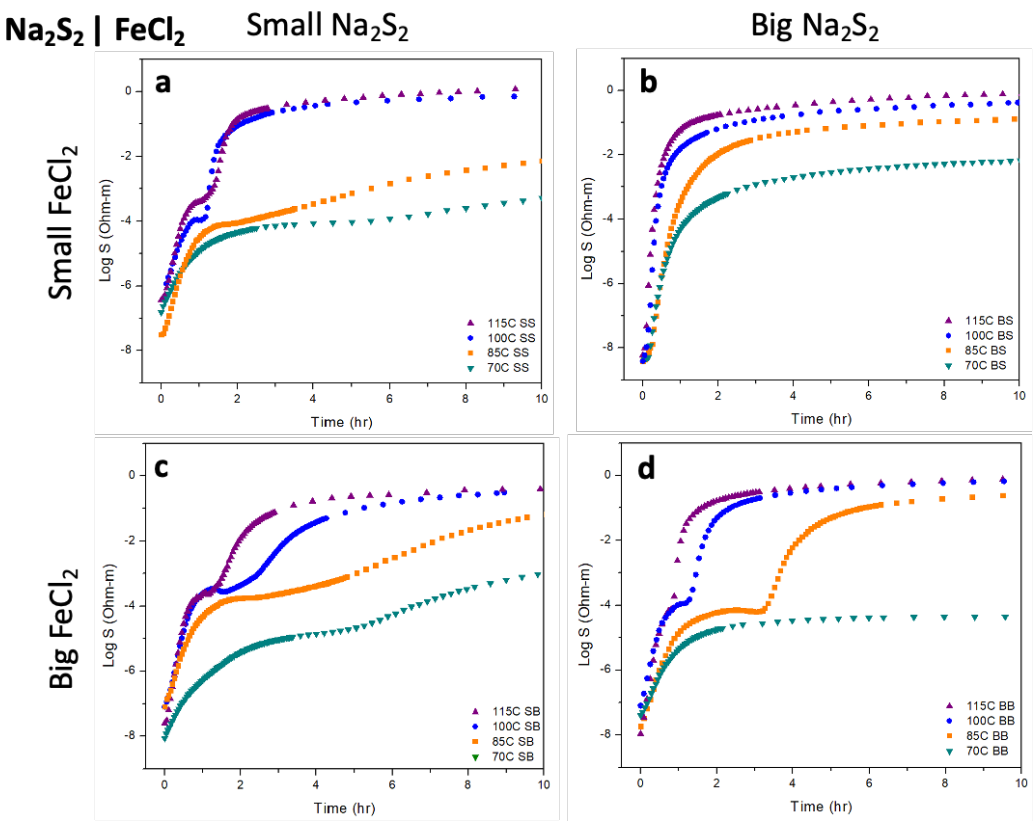

Figure 2.2: Graphs of log[conductivity] vs time during isothermal heating from 70-115°C for four different particle size scenarios (a) S/S small Na_2S_2 and small FeCl2, (b) B/S big Na_2S_2 and small $FeCl_2$, (c) S/B small Na_2S_2 and big $FeCl_2$ and (d) B/B big Na_2S_2 and big $FeCl_2$.

In all scenarios, conductivity rises quickly at the start of heating; at low temperatures (70°C), the conductivity appears to plateau after approximately 3 hrs. Raising the temperature decreases the length of this first plateau and the conductivity continues increasing before reaching a second plateau and stabilizing by the end of 10 hrs. This is most clearly seen in the B/B case (Figure 2d) where there is a sharp rise in conductivity at 3.5 hrs leading to a second plateau. At 115°C, the first plateau is shortened significantly, and conductivity proceeds to rapidly increase.

The rise in conductivity at temperatures below the formation temperature of FeS_2 (at ~245°C) can be attributed to the formation of conducting intermediate species such as $NaFeS_2$ at the interface. Literature shows a small amount of thermal energy is required for diffusion to initiate

NaCl formation, which has been observed at temperatures as low as 50°C.[37,38] As NaCl forms, Fe and S species start forming intermediates. At higher temperatures, it is concluded that NaCl forms more quickly since the first plateau shortens and finishes by ~1.5 hrs of heating. The larger amount of thermal energy helps push the completion of the intermediates and initiate formation of FeS_2 as evidenced by the higher conductivity values.

An interesting finding from comparing the effect of particle size is that while most scenarios experienced a plateau in conductivity, the combination of big Na_2S_2 with small $FeCl_2$ shows no first plateau and instead directly proceeds to the second plateau even at low temperatures. The small $FeCl_2$ particle size may aid the reaction in proceeding more rapidly than larger $FeCl_2$ particles due to Fe's known low mobility.[36,39] Previous work has shown that some of the first intermediates to form alongside NaCl include sodium-poor Na-S phases (Na_2S_4, Na_2S_5), sulfur-poor binary M-S phases (Fe_7S_8, Fe_3S_4) and a ternary $Na_3Fe_2S_4$.[40] Additionally, the $NaFeS_2$ intermediate has been realized as an anode material for sodium half cells due to its high electronic conductivity and layered structure[41], proving Na can readily be intercalated into $NaFeS_2$ and potentially contribute to progressing the reaction rapidly. Large Na_2S_2 particles may promote diffusion if the reaction becomes surface diffusion limited, such that the ions may travel more easily through bulk Na_2S_2 rather than the surfaces between Na_2S_2 and $FeCl_2$ particles. This may explain why having small particles of both Na_2S_2 and $FeCl_2$ may be deterring the reaction from proceeding as quickly.

One caveat of using impedance to monitor the conductivity of a product species is the difficulty in distinguishing the conductivity of intermediates from that of FeS_2. While the conductivity trends allow insight into conducting metastable intermediates, one must be careful not to attribute the entire conductivity value solely to the FeS_2 product.

2.3.2 100C Conductivity with XRD comparison

To investigate the first plateau, in-situ XRD is used to determine if any changes occur during the plateau at ~1hr of heating. The scenario of big Na_2S_2 and $FeCl_2$ particles (B/B) at 100°C isothermal heating is used to study possible changes occurring during both the first and second plateaus (Fig 3).

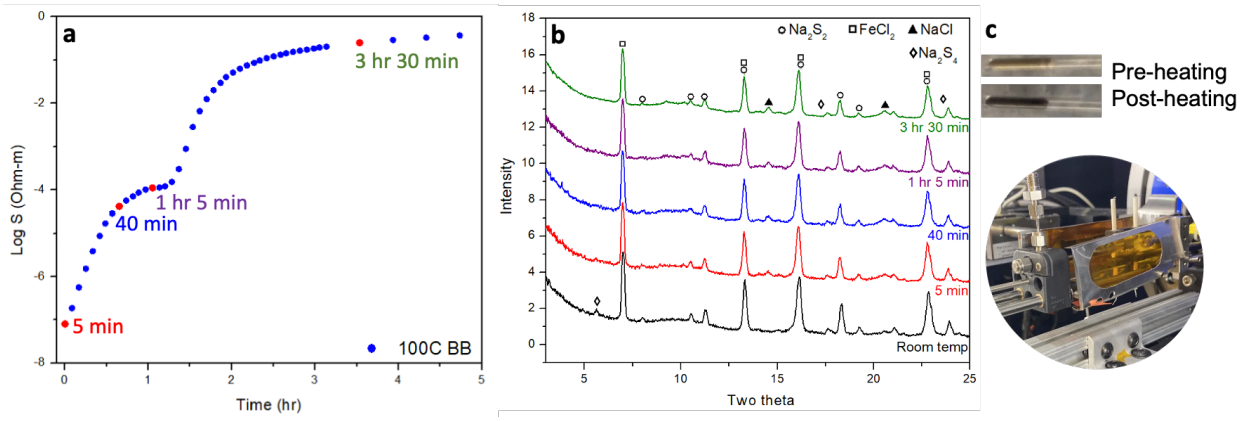

Figure 2.3: (a) Graph of log[conductivity] vs time during isothermal heating at 100°C for B/B big Na_2S_2 and big $FeCl_2$ scenario, (b) accompanying in-situ XRD while heating isothermally at 100°C, (c) photos of sample capillaries pre and post heating and experimental set-up.

XRD scans are taken every 5 min for 4 hrs while the sample is heated isothermally at 100°C. The main change is the formation of NaCl peaks at 14° and 20.5° during the first 10 minutes, beyond which there are no phase changes. Two main reasons may explain the change in conductivity and lack of change in XRD characterization: 1) new intermediates may be very amorphous with broad humps not detectable by XRD and 2) the amounts of new phases may be too small to be detectable by XRD. Because AC impedance relies on a conducting pathway between the two leads, the conductivity measurement is sensitive to any change occurring at the interface between particles. Therefore, any new conducting intermediates or products formed at the boundary between precursor particles can be detected and contribute to the overall conductivity measurement. Meanwhile, XRD is a bulk characterization technique which requires a phase to be

at least 3 wt % of the mixed sample to be detectable. Interestingly, the sample changes color from yellow to black after 10 hrs of heating at 100°C, showing that amorphous $NaFeS_2$ and FeS_2 may be quite conducting (and black) before the phases crystallize and become a significant enough weight percent to be detectable by XRD. Additionally, Na_2FeS_2 has been utilized as a new anode material for lithium ion batteries due to its high electronic conductivity.[41]

2.3.3 Diffusion controlled mechanism at later stages

At longer timescales (~3 hrs and longer for higher temperatures), the conductivity plateaus and shows smaller changes. To understand the kinetics in this regime, the JMAK equation, developed by Johnson, Mehl, Avrami and Kolmogorov is applied.[42–44] The JMAK equation (Eq. 2.4, 2.5) is a geometric model describing nucleation and growth in solid state reactions due to phase transformation.

$$x(t) = 1 - \exp(-kt^n) \qquad Eq.2.4$$

with

$$k(T) = k_o \exp\left(\frac{\Delta H}{k_B T}\right) \qquad Eq.2.5$$

The model describes the volume fraction of the transformed material, x, as a function of time during isothermal heating; n, k_o, and ΔH are JMAK parameters and k_B the Boltzmann constant. The JMAK equation incorporates parameters relating to nucleation and growth as well as dimensionality. This flexibility has led to many papers deriving a physical understanding of the Avrami exponent, n as it pertains to changing nucleation rates and diffusion-controlled regimes.[26,27,45,46]

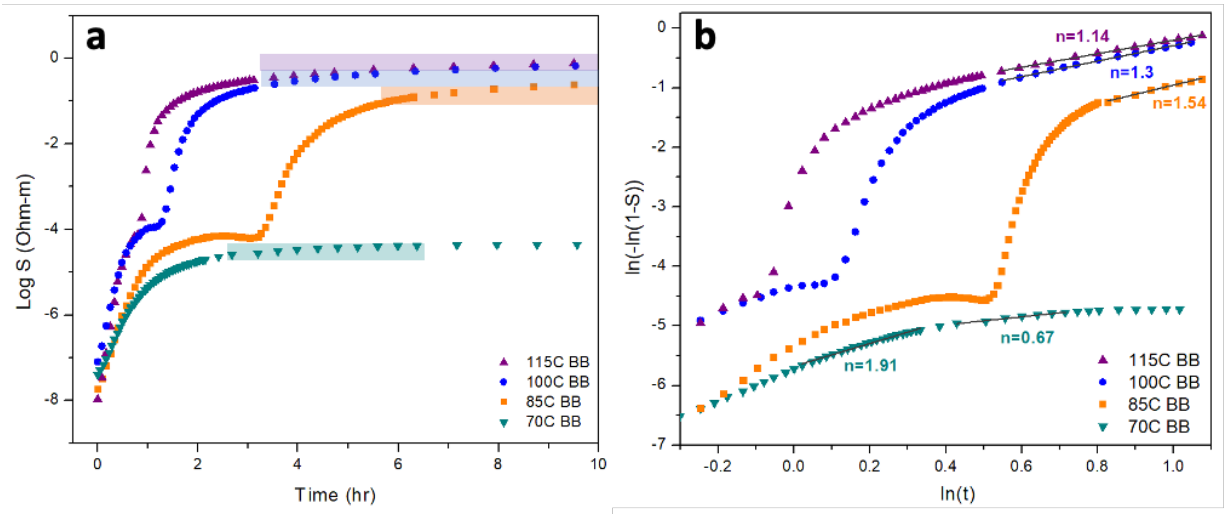

Figure 2.4: (a) Graph of log[conductivity] vs time during isothermal heating from 70-115°C for B/B big Na_2S_2 and big $FeCl_2$ scenario with shaded regions representing diffusion-limited regimes, analyzed with (b) Avrami plots showing a linear correlation with the slopes, n, representing the growth dimensionality in the JMAK model.

Assuming conductivity is representative of the fraction of transformed material, the Avrami exponent, n, is determined from the slope of ln[-ln(1-S)] vs ln[time] in the B/B scenario. At each isothermal hold, n is less than two, reflecting diffusion-limited one-dimensional growth of large particles.[47,48] Values of three and four are indicative of two and three-dimensional growth respectively. Interestingly, EDX mapping of a cross-section after being heated to 250°C shows new FeS_2 and NaCl formation sandwiched between the precursors akin to a one-dimension growth mechanism of large particles (SI). The general trend appears that n increases with decreasing temperature and is not a whole integer; n is 1.14 at 115°C, 1.3 at 100°C, and 1.54 at 85°C. Non-integer values such as 1.14 and 1.3 are considered to reflect decreasing nucleation rates as a function of time, showing the reactions at higher temperatures are slowing down as they approach saturation.[26,49] An n value of 1.54 at 100°C is only slightly smaller than 1.5, showing that this scenario is closer to having a constant nucleation rate and is diffusion controlled, according to Blazquez et al.[26]

During earlier times for the 70°C case, n has a higher value of 1.91, which closely resembles an interface-controlled regime (or growth edge nucleation) with a constant nucleation rate during which intermediates may still be forming. At later times, n becomes very low at 0.67, reflecting no more nucleation and a diffusion-controlled regime where large plates are thickening.[47] Beyond this point, the conductivity changes very little and it appears the system has reached saturation of maximum conductivity.

Additional analyses are conducted by plotting the conductivity with respect to time on a log-log scale and showing a linear relationship with a small slope indicative of a diffusion mechanism (Figure S4).

2.3.4 Conductivity and XRD comparison at 245°C

While AC impedance proves helpful in determining onset of reactions and quantifying intermediate pathways, its limitation comes when the conducting pathways have already formed and bulk changes affecting phase fraction become more dominant. In these circumstances, a bulk technique such as in-situ XRD becomes more appropriate. Measuring the conductivity at a higher temperature where FeS_2 is known to form (245°C) shows an expected steep rise in conductivity during the first 30 minutes of heating, after which any further changes cannot be detected by the EIS potentiostat (Figure 6a). In-situ XRD measurements during the same isothermal heating experiment provide more information on reaction mechanisms. There is a significant change in the first 5 minutes of heating, mainly due to NaCl formation and the concurrent $NaFeS_2$ intermediate phase that begins to form as the $FeCl_2$ precursor peaks decrease in intensity throughout the first 30 minutes (Figure 6d). In order to visualize the reaction progress, the change in area fraction under the first main peaks of NaCl and $FeCl_2$ is plotted in conjunction with the conductivity change

throughout the first hour, showing the same trend in opposing directions of rapidly decreasing $FeCl_2$ amounts and increasing NaCl amounts as the conductivity dramatically rises and plateaus (Figure 6b). The changes become more gradual as the Na_2S_2 and $FeCl_2$ precursor peaks decrease in intensity and NaCl, $NaFeS_2$ and Fe_7S_8 intermediate peaks grow (Figure 6c).

By the end of 5 hours, most of the peaks present correspond to NaCl, however there are also smaller peaks that match $NaFeS_2$ still present. FeS_2 peaks are also present but are hard to deconvolute from the still-present intermediates and NaCl. This may imply that FeS_2 first forms as small amorphous regions before significant diffusion and time helps convert the remaining $NaFeS_2$ intermediate to growing FeS_2 crystalline regions. Previous work done on this metathesis reaction held the reaction at temperature for 24 hours before measuring FeS_2 peaks, suggesting that additional time in addition to higher temperatures may also be required for a more complete reaction.[37]

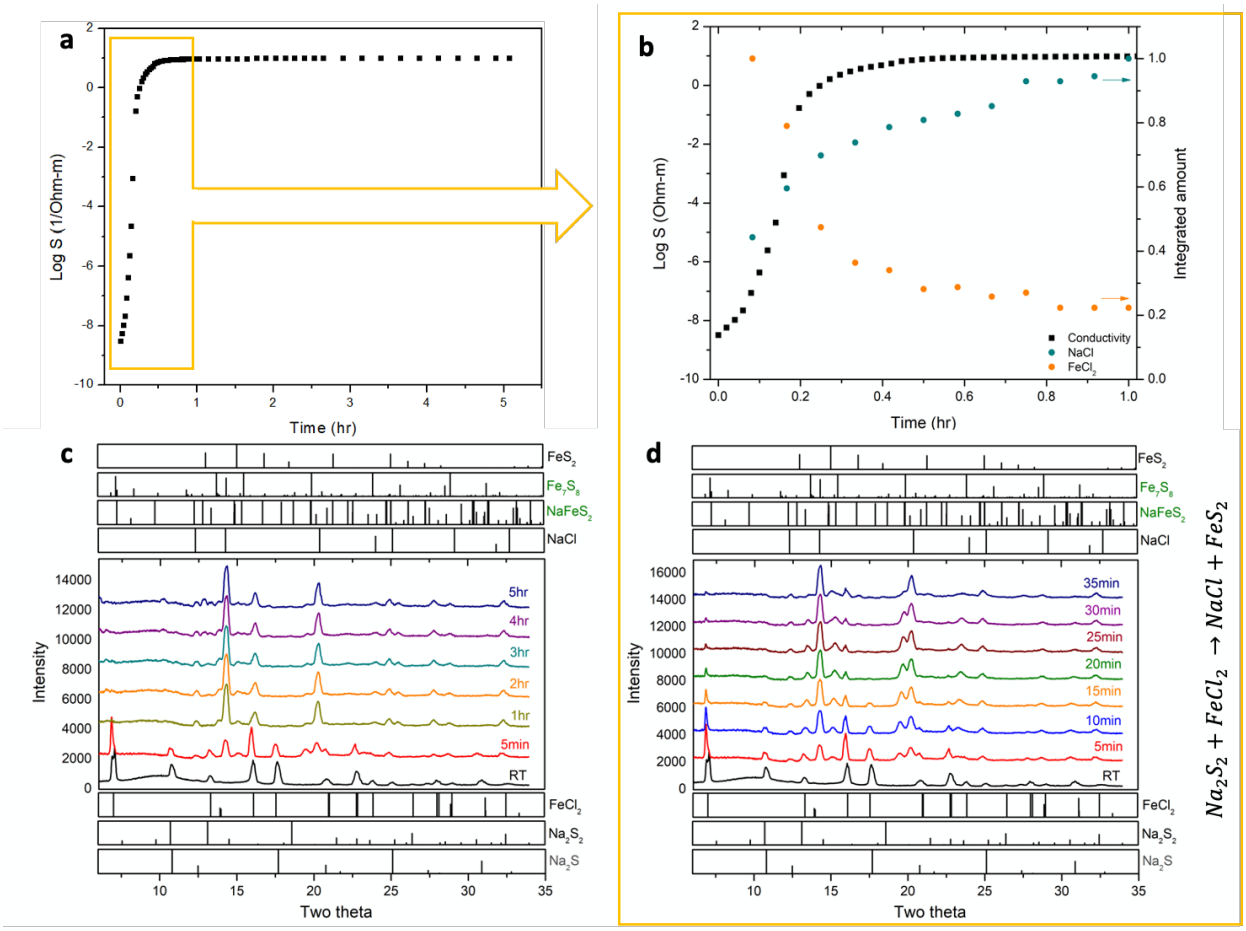

Figure 2.5: (a) Graph of log[conductivity] vs time during isothermal heating at 245°C for B/B big Na_2S_2 and big $FeCl_2$ scenario with (b) the first hour magnified and area fraction of increasing NaCl and decreasing $FeCl_2$ amounts obtained from XRD measurements. In-situ XRD scans taken during isothermal heating are shown for the first 5 hours (c) and magnified for the first 35 minutes (d). ICSD peak positions of precursors are shown below the XRD plots and products (NaCl and FeS_2 in black) and intermediates (Fe_7S_8 and $NaFeS_2$ in green) are shown above.

Additionally, SEM and EDX mapping can be used as complementary tools in understanding the homogeneity and morphology of the sample. While EDX mapping has a resolution limit on the micron scale such that minute changes at the interface are hard to probe, post-mortem mapping shows the significant overlap of Fe/S and Na/Cl elements implying the formation of FeS_2 and NaCl products at their interface (Figure S3).

2.4 Conclusions

In conclusion, this work presents a novel method of characterizing and monitoring in-situ solid state reaction using impedance spectroscopy. In particular, the FeS_2 metathesis reaction is studied under varying isothermal conditions, showing changes in reaction kinetics based on particle size effects. In most cases, as the reaction progresses, conductivity increases until it reaches a small plateau, before it continues rising to a second plateau and reaching saturation. Because the conductivity measurements are incredibly sensitive to interfacial change, they can detect the onset of reaction before XRD measurements can. Assuming a two-step reaction, the conductivity data can then be modeled as a first order reaction and quantitative activation energies can be determined for each step. During longer times, the conductivity data follows a diffusion-limited model. XRD measurements can then be used to complement conductivity data at higher temperatures where there is a larger amount of product growth and formation to determine reaction mechanisms and intermediates.

2.5 Acknowledgments

Chapter 2, in part is currently being prepared for submission for publication of the material, V. Petrova**,** E. Maria, J. Ferrari, G. Kamm, J. Neilson, K. Thornton, K. Chapman, P. Liu. The dissertation author was the primary researcher and author of this material.

SUPPLEMENTAL INFORMATION:

1. **XRD Na_2S_2**

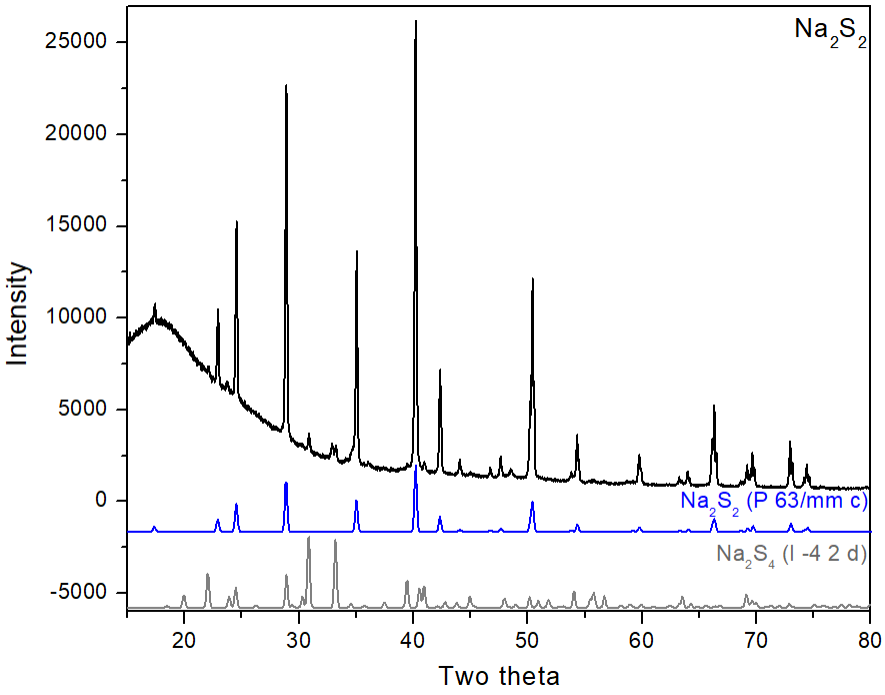

Figure 2.6: XRD of synthesized Na_2S_2 showing main peaks corresponding to Na_2S_2 (P 63/mm c) with minor contributions from Na_2S_4 (I -4 2 d).

2. **Conductivity trends during temperature ramping to 250C as function of particle size**

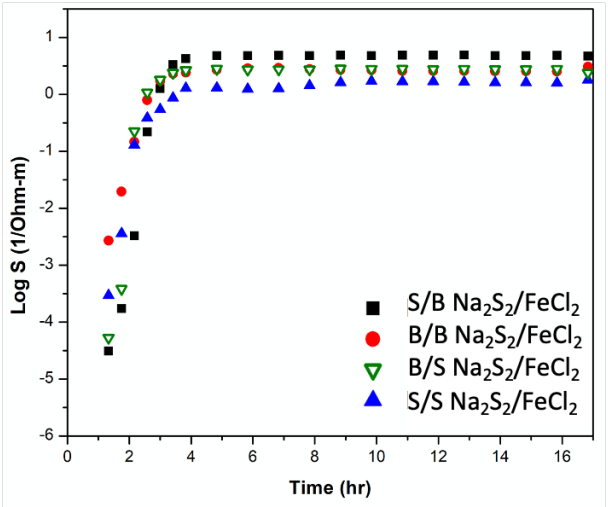

Figure 2.7: Log[conductivity] vs time with varying particle size at 250C

3. SEM and EDX of cross-section, post-mortem, 250C

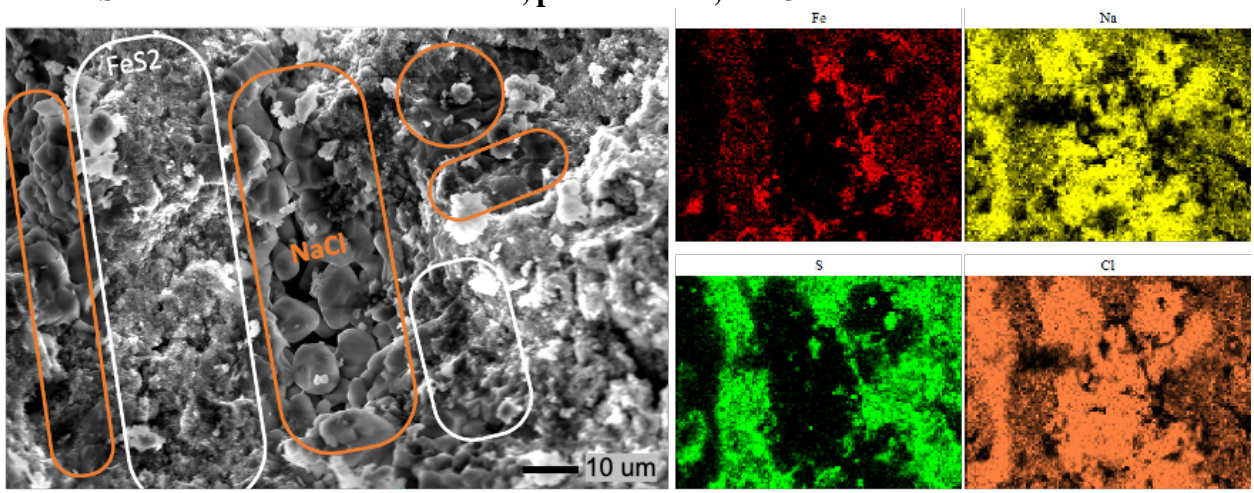

Figure 2.8: Cross-sectional SEM with EDX mapping showing post-mortem product formation

REFERENCES:

(1) Kohlmann, H. Looking into the Black Box of Solid-State Synthesis. *Eur. J. Inorg. Chem.* **2019**, *2019* (39–40), 4174–4180. https://doi.org/10.1002/ejic.201900733.

(2) Stein, A.; Keller, S. W.; Mallouk, T. E. Turning Down the Heat: Design and Mechanism in Solid-State Synthesis. *Science (80-.).* **1993**, *259* (9), 1558–1563.

(3) Disalvo, F. J. Solid-State Chemistry: A Rediscovered Chemical Frontier. *Science (80-.).* **1990**, *247* (4943), 649–655. https://doi.org/10.1126/science.247.4943.649.

(4) Schafer, H. Preparative Solid State Chemistry: The Present Position. *Angew. Chem. Int. Ed* **1971**, *10*, 43–50.

(5) Shoemaker, D. P.; Hu, Y. J.; Chung, D. Y.; Halder, G. J.; Chupas, P. J.; Soderholm, L.; Mitchell, J. F.; Kanatzidis, M. G. In Situ Studies of a Platform for Metastable Inorganic Crystal Growth and Materials Discovery. *Proc. Natl. Acad. Sci. U. S. A.* **2014**, *111* (30), 10922–10927. https://doi.org/10.1073/pnas.1406211111.

(6) Chupas, P. J.; Ciraolo, M. F.; Hanson, J. C.; Grey, C. P. In Situ X-Ray Diffraction and Solid-State NMR Study of the Fluorination of γ-Al2O3 with HCF2Cl. *J. Am. Chem. Soc.* **2001**, *123* (8), 1694–1702. https://doi.org/10.1021/ja0032374.

(7) Chen, Z.; Ren, Y.; Qin, Y.; Wu, H.; Ma, S.; Ren, J.; He, X.; Sun, Y. K.; Amine, K. Solid State Synthesis of LiFePO4 Studied by in Situ High Energy X-Ray Diffraction. *J. Mater. Chem.* **2011**, *21* (15), 5604–5609. https://doi.org/10.1039/c0jm04049e.

(8) Weber, R.; Li, H.; Chen, W.; Kim, C.-Y.; Plucknett, K.; Dahn, J. R. In Situ XRD Studies During Synthesis of Single-Crystal LiNiO 2 , LiNi 0.975 Mg 0.025 O 2 , and LiNi 0.95 Al 0.05 O 2 Cathode Materials . *J. Electrochem. Soc.* **2020**, *167* (10), 100501. https://doi.org/10.1149/1945-7111/ab94ef.

(9) Yalfani, M. S.; Santiago, M.; Pérez-Ramírez, J. In Situ Studies during Thermal Activation of Dawsonite-Type Compounds to Oxide Catalysts. *J. Mater. Chem.* **2007**, *17* (12), 1222–1229. https://doi.org/10.1039/b615264c.

(10) Jones, A. R.; Winter, R.; Florian, P.; Massiot, D. Tracing the Reactive Melting of Glass-Forming Silicate Batches by in Situ23Na NMR. *J. Phys. Chem. B* **2005**, *109* (10), 4324–4332. https://doi.org/10.1021/jp045705s.

(11) El Hajraoui, K.; Luong, M. A.; Robin, E.; Brunbauer, F.; Zeiner, C.; Lugstein, A.; Gentile, P.; Rouvière, J. L.; Den Hertog, M. In Situ Transmission Electron Microscopy Analysis of Aluminum-Germanium Nanowire Solid-State Reaction. *Nano Lett.* **2019**, *19* (5), 2897–2904. https://doi.org/10.1021/acs.nanolett.8b05171.

(12) McDermott, M. J.; Dwaraknath, S. S.; Persson, K. A. A Graph-Based Network for Predicting Chemical Reaction Pathways in Solid-State Materials Synthesis. *Nat. Commun.* **2021**, *12* (1), 1–12. https://doi.org/10.1038/s41467-021-23339-x.

(13) Vadhva, P.; Hu, J.; Johnson, M. J.; Stocker, R.; Braglia, M.; Brett, D. J. L.; Rettie, A. J. E. Electrochemical Impedance Spectroscopy for All-Solid-State Batteries: Theory, Methods and Future Outlook. *ChemElectroChem* **2021**, *8* (11), 1930–1947. https://doi.org/10.1002/celc.202100108.

(14) Fielder, W. L.; Singer, J. Solubility, Stability, and Electrochemical Studies of Sulfur-Sulfide. *NASA Tech. Pap.* **1978**, No. August, 1–40.

(15) Laschuk, N. O.; Easton, E. B.; Zenkina, O. V. Reducing the Resistance for the Use of Electrochemical Impedance Spectroscopy Analysis in Materials Chemistry. *RSC Adv.* **2021**, *11* (45), 27925–27936. https://doi.org/10.1039/d1ra03785d.

(16) Hui, Z.; Mayilvahanan, K. S.; Yang, Y.; West, A. C. Determining the Length Scale of Transport Impedances in Li-Ion Electrodes: Li(Ni 0.33 Mn 0.33 Co 0.33)O 2 . *J. Electrochem. Soc.* **2020**, *167* (10), 100542. https://doi.org/10.1149/1945-7111/ab9cce.

(17) Mwizerwa, J. P.; Zhang, Q.; Han, F.; Wan, H.; Cai, L.; Wang, C.; Yao, X. Sulfur-Embedded FeS2as a High-Performance Cathode for Room Temperature All-Solid-State Lithium-Sulfur Batteries. *ACS Appl. Mater. Interfaces* **2020**, *12* (16), 18519–18525. https://doi.org/10.1021/acsami.0c01607.

(18) Kaur, G.; Kaur, M.; Thakur, A.; Kumar, A. *Recent Progress on Pyrite FeS2 Nanomaterials for Energy and Environment Applications: Synthesis, Properties and Future Prospects*; Springer US, 2020; Vol. 31. https://doi.org/10.1007/s10876-019-01708-3.

(19) Dewald, G. F.; Liaqat, Z.; Lange, M. A.; Tremel, W.; Zeier, W. G. Influence of Iron Sulfide Nanoparticle Sizes in Solid-State Batteries**. *Angew. Chemie - Int. Ed.* **2021**, *60* (33), 17952–17956. https://doi.org/10.1002/anie.202106018.

(20) McAuliffe, R. D.; Petrova, V.; McDermott, M. J.; Tyler, J. L.; Self, E. C.; Persson, K. A.; Liu, P.; Veith, G. M. Synthesis of Model Sodium Sulfide Films. *J. Vac. Sci. Technol. A Vacuum, Surfaces, Film.* **2021**, *39* (5). https://doi.org/10.1116/6.0001069.

(21) Chupas, P. J.; Chapman, K. W.; Kurtz, C.; Hanson, J. C.; Lee, P. L.; Grey, C. P. A Versatile Sample-Environment Cell for Non-Ambient X-Ray Scattering Experiments. *J. Appl. Crystallogr.* **2008**, *41* (4), 822–824. https://doi.org/10.1107/S0021889808020165.

(22) Yue, X.; He, Q.; Lim, H.-D.; Liu, P. Hierarchical Structural Designs of Ion Exchange Membranes for Flow Batteries. *J. Mater. Chem. A* **2019**, *7* (10), 5794–5802. https://doi.org/10.1039/C8TA11974K.

(23) Khawam, A.; Flanagan, D. R. Solid-State Kinetic Models: Basics and Mathematical Fundamentals. *J. Phys. Chem. B* **2006**, *110* (35), 17315–17328. https://doi.org/10.1021/jp062746a.

(24) Bondioli, F.; Bonamartini Corradi, A.; Ferrari, A. M.; Manfredini, T.; Pellacani, G. G. Kinetic Study of Conventional Solid-State Synthesis of BaTiO3 by in Situ HT-XRD.

Mater. Sci. Forum **1998**, *278–281* (PART 1), 379–383. https://doi.org/10.4028/www.scientific.net/msf.278-281.379.

(25) Shirzad, K.; Viney, C. A Critical Review on Applications of the Avrami Equation beyond Materials Science. *J. R. Soc. Interface* **2023**, *20* (203). https://doi.org/10.1098/rsif.2023.0242.

(26) Blázquez, J. S.; Romero, F. J.; Conde, C. F.; Conde, A. A Review of Different Models Derived from Classical Kolmogorov, Johnson and Mehl, and Avrami (KJMA) Theory to Recover Physical Meaning in Solid-State Transformations. *Phys. Status Solidi Basic Res.* **2022**, *259* (6). https://doi.org/10.1002/pssb.202100524.

(27) Ruitenberg, G.; Woldt, E.; Petford-Long, A. K. Comparing the Johnson-Mehl-Avrami-Kolmogorov Equations for Isothermal and Linear Heating Conditions. *Thermochim. Acta* **2001**, *378* (1–2), 97–105. https://doi.org/10.1016/S0040-6031(01)00584-6.

(28) Weinberg, M. C.; Birnie, D. P.; Shneidman, V. A. Crystallization Kinetics and the JMAK Equation. *J. Non. Cryst. Solids* **1997**, *219*, 89–99. https://doi.org/10.1016/S0022-3093(97)00261-5.

(29) BERETKA, J. Kinetic Analysis of Solid-state Reactions Between Powdered Reactants. *J. Am. Ceram. Soc.* **1984**, *67* (9), 615–620. https://doi.org/10.1111/j.1151-2916.1984.tb19605.x.

(30) Galdikas, A.; Usman, M.; Galdikas, M. The Kinetic Model of Diffusion and Reactions in Powder Catalysts during Temperature Programmed Oxygen Isotopic Exchange Process. *Symmetry (Basel).* **2021**, *13* (8), 1–14. https://doi.org/10.3390/sym13081526.

(31) Acharyya, P.; Sarkar, D.; Dutta, P.; Biswas, K. *Metal Chalcogenide Materials: Synthesis, Structure and Properties*; Elsevier, 2023; Vol. 5. https://doi.org/10.1016/b978-0-12-823144-9.00150-3.

(32) Martin, J. D. Particle Size Is a Primary Determinant for Sigmoidal Kinetics of Nanoparticle Formation: A "Disproof" of the Finke-Watzky (F-W) Nanoparticle Nucleation and Growth Mechanism. *Chem. Mater.* **2020**, *32* (8), 3651–3656. https://doi.org/10.1021/acs.chemmater.9b02839.

(33) Shimizu, A.; Hao, Y. J. Prediction of Powder Reaction Rate from Hao-Tanaka's Model. *Adv. Powder Technol.* **1991**, *2* (2), 103–109. https://doi.org/10.1016/S0921-8831(08)60710-4.

(34) Carter, R. E. Kinetic Model for Solid - State Reactions □. **2015**, *2015* (1961), 2010–2015.

(35) Coaty, C. M.; Corrao, A. A.; Petrova, V.; Khalifah, P. G.; Liu, P. Morphological Tuning of Nanoporous Metals Prepared with Conversion Reaction Synthesis via Thermal Annealing. *J. Phys. Chem. C* **2019**, *123* (29). https://doi.org/10.1021/acs.jpcc.9b04172.

(36) Wang, F.; Robert, R.; Chernova, N. A.; Pereira, N.; Hua, X.; Ruotolo, M.; Zhang, R.; Wu,

L.; Volkov, V.; Su, D.; Key, B.; Whittingham, ^ M Stanley; Grey, C. P.; Amatucci, G. G.; Zhu, Y.; Graetz, J. Conversion Reaction Mechanisms in Lithium Ion Batteries: Study of the Binary Metal Fluoride Electrodes. *J. Am. Chem. Soc* **2011**, *133*, 18828–18836. https://doi.org/10.1021/ja206268a.

(37) Martinolich, A. J.; Neilson, J. R. Pyrite Formation via Kinetic Intermediates through Low-Temperature Solid-State Metathesis. *J. Am. Chem. Soc.* **2014**, *136* (44), 15654–15659. https://doi.org/10.1021/ja5081647.

(38) Halperin, A.; Braner, A. A.; Ben-Zvi, A.; Kristianpoller, N. Thermal Activation Energies in NaCl and KCl Crystals. *Phys. Rev.* **1960**, *117* (2), 416–422. https://doi.org/10.1103/PhysRev.117.416.

(39) Wu, F.; Yushin, G. Conversion Cathodes for Rechargeable Lithium and Lithium-Ion Batteries. *Energy Environ. Sci.* **2017**, *10* (2), 435–459. https://doi.org/10.1039/c6ee02326f.

(40) Martinolich, A. J.; Kurzman, J. A.; Neilson, J. R. Circumventing Diffusion in Kinetically Controlled Solid-State Metathesis Reactions. *J. Am. Chem. Soc.* **2016**, *138* (34), 11031–11037. https://doi.org/10.1021/jacs.6b06367.

(41) Zhang, J.; Li, T.; Li, B.; Zhang, S.; Dou, Y.; Yuan, Q.; Wu, Y.; Han, J. Erdite NaFeS2as a New Anode Material for Lithium-Ion Batteries. *ACS Sustain. Chem. Eng.* **2022**, *10* (32), 10666–10674. https://doi.org/10.1021/acssuschemeng.2c02806.

(42) Avrami, M. Kinetics of Phase Change. I: General Theory. *J. Chem. Phys.* **1939**, *7* (12), 1103–1112. https://doi.org/10.1063/1.1750380.

(43) Suo, Z. Lecture 6 Surface Diffusion Driven by Surface Energy. **2004**, 1–11.

(44) Park, C. L.; Voorhees, P. W.; Thornton, K. Evolution of Interfacial Curvatures of a Bicontinuous Structure Generated via Nonconserved Dynamics. *Acta Mater.* **2015**, *90*, 182–193. https://doi.org/10.1016/j.actamat.2015.02.037.

(45) Ranganathan, S.; Von Heimendahl, M. The Three Activation Energies with Isothermal Transformations: Applications to Metallic Glasses. *J. Mater. Sci.* **1981**, *16* (9), 2401–2404. https://doi.org/10.1007/BF01113575.

(46) Pérez-Maqueda, L. A.; Criado, J. M.; Sánchez-Jiménez, P. E. Combined Kinetic Analysis of Solid-State Reactions: A Powerful Tool for the Simultaneous Determination of Kinetic Parameters and the Kinetic Model without Previous Assumptions on the Reaction Mechanism. *J. Phys. Chem. A* **2006**, *110* (45), 12456–12462. https://doi.org/10.1021/jp064792g.

(47) G.F. Janssens, K.; Raabe, D.; Kozeschnik, E.; A. Miodownik, M.; Nestler, B. Computational Materials Engineering. *Elsevier Acad. Press* **2007**.

(48) Christian, J. W. *The Theory of Transformations in Metals and Alloys*; 2002.

(49) Bertmer, M.; Nieuwendaal, R. C.; Barnes, A. B.; Hayes, S. E. Solid-State Photodimerization Kinetics of α-Trans-Cinnamic Acid to α-Truxillic Acid Studied via Solid-State NMR. *J. Phys. Chem. B* **2006**, *110* (12), 6270–6273. https://doi.org/10.1021/jp057417h.

CHAPTER 3: SYNTHESIS OF FLEXIBLE CO NANOWIRES FROM BULK PRECURSORS

3.1 Introduction

1D nanostructures offer a unique opportunity to study electronic, plasmonic, magnetic, electrical, mechanical, and thermal properties of materials to enable a wide range of applications. Metal nanowires (NWs) have electrical properties and a flexible structure that can be utilized for flexible solar cells and touch screens while NWs with magnetic properties can be used for thin film magnets with high energy density, spintronic circuits and sensors.[1–7] While metal alloy compounds experience low resistance to aggressive external factors such as temperature, oxygen and electromagnetic radiation; the class of iron oxide ferrites are much more stable when used up to 1000°C and maintain excellent electronic properties.[8,9] Additionally, work done on metal-based NWs shows the importance of NW geometries on their magnetic properties.[10,11]

The synthesis of 1D nanostructures generally employs either a top-down or a bottom-up approach. A top-down approach uses templates such as anodized alumina to confine the growth inside the channels.[12] In bottom-up solution-based synthesis, ligands or surfactants are employed to encourage the growth of the solid phase in a specific direction while vapor-phase growth involves the use of catalysts to seed the growth.[2,13] Examples of bottom-up synthesis include using sol-gel approaches and rhizome plant extracts.[14,15] Although the scalability of these methods has advanced significantly in recent years, it would be highly desirable to synthesize 1D nanostructures from bulk, solid precursors without the need of additional structural guiding agents. Such processes would be highly scalable and robust, with the potential to offer low-cost 1D nanomaterials in large quantities.

Examples of nanowire (NW) formation from decomposition of bulk precursors without assistance from templates, ligands, or catalysts are rare.[16] Previously, aluminum metal-organic NWs were formed by exposing AlLi alloy particles to alcohol, dissolving out the Li alkoxide and forming $Al(EtOH)_3$ NWs.[17,18] The proposed formation mechanism is a

minimization of strain energy at the boundary of the chemical reaction front. However, there are so far no simple methods of easily producing metal NWs from bulk precursors. Most fcc metals have a strong tendency to reduce their total surface energy by taking a highly symmetric shape during growth, and therefore do not grow in nanowire forms without templates or structural directing agents.

We report a simple, scalable method of producing flexible Co NWs directly from bulk precursors at room temperature. We have previously shown a process in which a metal halide undergoes a conversion reaction with *n*-butyllithium to form a nanocomposite of the metal and halide salt. The salt is then removed through dissolution in methanol, leaving behind an isotropic nanoporous metal.[19] Here, we show that diluting the precursor metal halide by using the Suzuki phase Li_6CoCl_8 results in a new NW morphology. When the Suzuki phase reacts with *n*-butyllithium, a nanocomposite of Co in a LiCl matrix is formed. Upon removing the LiCl salt with methanol, the Co atoms migrate and are extruded from the matrix as NWs (Eq. 3.1, Figure 3.1).

$$Li_6CoCl_8 + 2BuLi \rightarrow 8LiCl + Co \Rightarrow Co\ (NWs) \qquad \text{Eq. 3.1}$$

This work introduces a more efficient and simple synthesis procedure of producing Co NWs from bulk precursors. Understanding how to control morphology based on material properties can provide design guidelines to synthesize and tailor the morphology of nanomaterials.

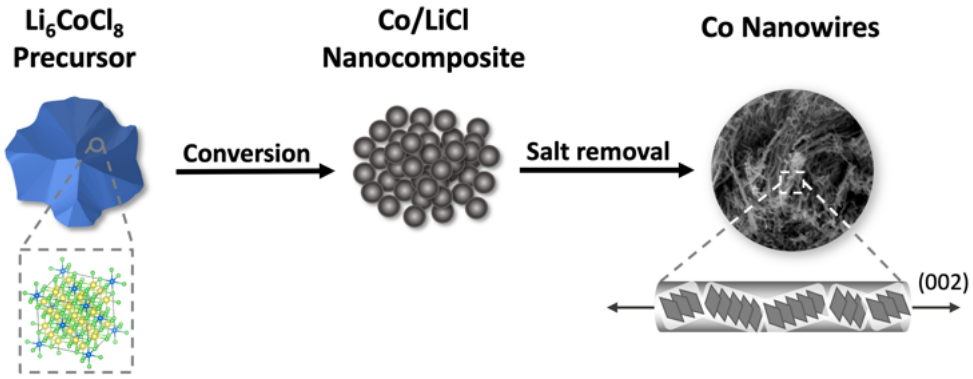

Figure 3.1: Schematic of synthesis procedure for producing Co NWs. Li_6CoCl_8 first undergoes a conversion reaction with n-BuLi to form a nanocomposite, from which the salt is removed to leave Co NWs.

3.2 Experimental Methods

Li_6CoCl_8, Li_2CoCl_4, and Li_6NiCl_8 precursors are synthesized through a solid-state process as described in literature.[20–22] Stoichiometric ratios of anhydrous $CoCl_2$ or $NiCl_2$ (98% Sigma-Aldrich) and LiCl (99% Sigma Aldrich) are ground using a mortar and pestle for 10 min in an argon glovebox and then vacuum sealed in a glass ampoule. The combined $CoCl_2$ and LiCl powders are heated at 400°C and 315°C for seven days to form Li_6CoCl_8 and Li_2CoCl_4 respectively. The combined $NiCl_2$ and LiCl powder is heated at 540°C for seven days to form Li_6NiCl_8. The Li_6CoCl_8, Li_2CoCl_4 and Li_6NiCl_8 precursors are then cooled to room temperature and stored in an argon glovebox (<10 ppm O_2). It is imperative that the precursors are pure and dry since both chloride salts are very hygroscopic and can easily introduce impurities if exposed to atmospheric conditions.

The precursor is converted into a nanocomposite following a published procedure.[19] The precursor is first ground with mortar and pestle and sieved so that particles are homogenous and smaller than 150 um. 1 g of precursor is then reacted with x1.5 excess 0.05 M *n*-butyllithium (from 1.6 M in hexane, Sigma-Aldrich and further diluted with hexane, HPLC, Fisher Scientific) for seven days. The resulting nanocomposite powder is isolated by rinsing with hexane with a filter funnel under vacuum and allowed to dry overnight at room temperature. The nanocomposite is further rinsed with methanol (HPLC, sparged with Argon for 1 hr and desiccated with molecular sieves, Type 3A, Sigma Aldrich) five times to remove the LiCl salt. Since methanol has a high volatility, drying the final product overnight at room temperature in the glovebox is sufficient to obtain a fully dry final product. The conversion and salt removal processes take place in a glovebox. The writing of these methods is structured so that natural language processing can

extract data and easily create a synthesis flow chart for future applications in building databases for materials synthesis machine learning.[23]

Experimental details and equipment parameters regarding sample preparation for XRD and SEM characterization can be found in the Supporting Information.

3.3 Results and Discussion

3.3.1 X-ray diffraction

The synthesized Suzuki phase Li_6CoCl_8 has a rocksalt crystal structure (*Fm-3m*) confirmed by X-ray diffraction (Figure 3.2a) and is a superstructure of LiCl with lattice parameters twice those of LiCl and an ordered arrangement of cations and vacancies over octahedral sites.

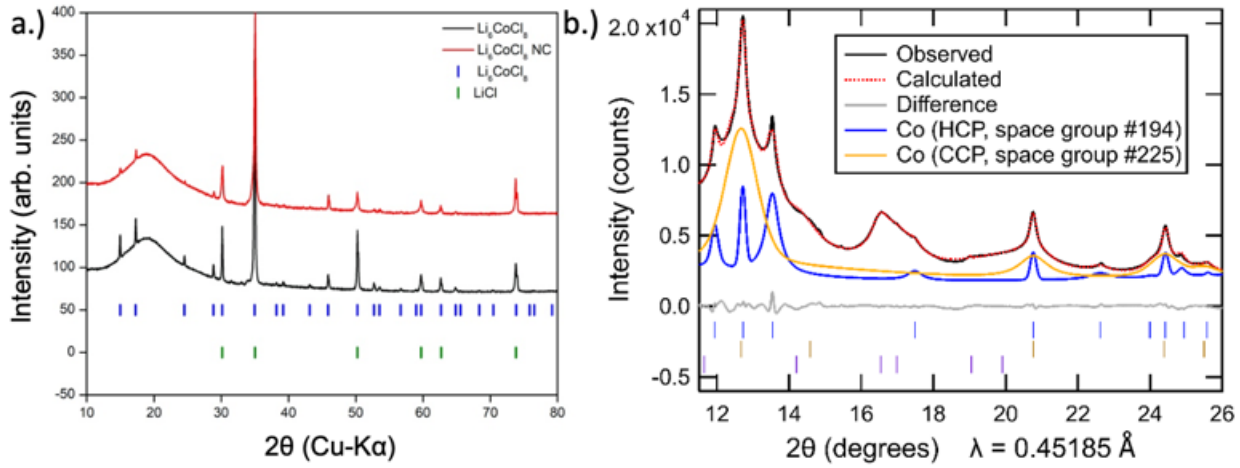

Figure 3.2: a.) Laboratory XRD patterns of synthesized Li_6CoCl_8 (black) and nanocomposite (red) with markers of literature peak positions of Li_6CoCl_8 (blue) and LiCl (green). b.) Synchrotron diffraction pattern of Co NWs (black) with the simulated pattern (red) of an hcp (26%, blue) and ccp (74%, orange) Co mixture. Markers are shown for six minor unindexed peaks (purple), with further details in Figure S4.

The nanocomposite formed after reaction with *n*-butyllithium for seven days shows the disappearance of certain Suzuki peaks (2θ = 38.2, 39.2, 43.1), the significant decrease in intensity of other Suzuki peaks as well as the appearance of peaks of LiCl (Figure 3.2a). Because the Suzuki phase is a superstructure of LiCl, the Li_6CoCl_8 sub-cell peaks correspond to the same interplanar distances as the LiCl peaks and are nearly exactly overlapped, thus reaction progress is primarily

determined by changes in the Suzuki peaks. While the minor residual Suzuki peaks indicate the reaction may not have proceeded to completion, any precursor left in the nanocomposite is soluble and removed in the methanol dissolution step and therefore does not affect the formation of NWs. Further experiments on longer reaction times (30 days) show a fully converted precursor with the same resulting NW morphology (Supporting Information S1). Full conversion is exceedingly slow due to the diluted Co precursor as Li_6CoCl_8; this slow rate is likely a result of the small volume change that affects the reaction propagation. Estimation of volume change from precursor to nanocomposite based on Eq. 1 is 3.5%. In comparison, $CoCl_2$ experiences a 23% volume expansion and full conversion occurs on the order of hours.[19] The small volume change will discourage a reaction mechanism involving particle fracture and infusion of butyllithium. During the lithiation process, the reaction front is hypothesized to occur through extrusion, similar to the lithiation of FeF_3 in which Li insertion and Fe extrusion occur concurrently but the fluoride lattice remains coherent.[24] Here the virtually identical structure of LiCl and Li_6CoCl_8 makes a similar mechanism also likely.

While laboratory XRD is sufficient to determine the Suzuki phase and analyze changes during conversion, synchrotron XRD is required to fully resolve the cobalt phases in the NWs, as is shown in previous work done on ZnO/Co nanoporous metals.[25] Lab XRD of the Co NWs only shows a broad Co peak due to the extremely small nanoscale Co domains (Supporting Information S2).

Synchrotron X-ray powder diffraction studies show that the final nanowire product contains a mixture of two different cobalt polymorphs as well as a minor contribution from at least one as-yet unindexed phase with all three components exhibiting broad peaks (Figure 3.2b). While bulk Co is typically found in its cubic close packed (ccp) form, a hexagonal close packed (hcp)

polymorph has previously been reported to be more stable at low temperatures, and nanoparticles of cobalt commonly exhibit a mixture of hcp and ccp polymorphs[26], one or both of which may contain stacking faults.[27,28] Powder diffraction methods are frequently used to obtain quantitative insights into phase fractions (based on the pattern of peak intensities) and into sample size and strain (based on the peak profiles), information which is of interest for the present nanowire samples.

Initial efforts to model the Co nanowires diffraction pattern through Rietveld refinements where the peak shapes of hcp Co and ccp Co follow conventional models of isotropic size and/or strain broadening resulted in poor fits (Supporting Information S3a), as evidenced by the large refinement R_{wp} of 11.9% for the optimal parameter choices. The problems in the fitting persisted even when utilizing Pawley methods which allowed the peak intensities of these phases to be freely refined (R_{wp} = 2.5%, Supporting Information S3b), further supporting the conclusion that the primary challenge in the refinement is properly describing the sample peak shape. Attempts to improve the fitting of diffraction peaks in Rietveld refinements using anisotropic strain broadening[29] and anisotropic size broadening[30,31] models in which the peak shapes are *hkl*-dependent were similarly unsuccessful.

We therefore developed a novel approach for Rietveld refinement in which the pseudo-Voigt shape of each *hkl* peak was independently refined using custom TOPAS macros written for this purpose. This allowed the intensities of all the peaks for the hcp and ccp polymorphs to be fully constrained by their conventional structural model (with the isotropic displacement parameter of Co additionally constrained to be the same in both phases). Even within these strong constraints, it was possible to obtain a far better fit (R_{wp} = 1.9%, Supporting Information S3c) than the other conventional approaches. The refined lattice parameters and crystallographic parameters of the

two Co phases are provided in the SI, together with information in Table S2 about the unindexed peaks that were utilized in the same manner for all the fits shown in Supporting Information S3. The need to use independent peak shape parameters for each peak suggests that the nanoscale domains of the hcp and ccp have shapes which are strongly anisotropic or irregular. The much broader peaks of the ccp phase indicate that its domain size is significantly smaller than that of the hcp phase. While the shape anisotropy suggests that the size cannot be captured using a single dimension, the refined size parameters of 5 nm (hcp) and 1.6 nm (ccp) approximated from Pawley fits using an isotropic size broadening model (Supporting Information Table S3) provide a sense of the relative scale of the domains of these two Co polymorphs. The large breadths of the unindexed peaks (Supporting Information S4) are comparable to that of the ccp Co phase, suggesting that these unindexed peaks may be associated with a thin surface layer on Co associated with surface oxidation or another decomposition reaction. A thin surface layer may be constrained by the underlying metal, perhaps preventing this phase from adopting a known structure type and thus hindering efforts to index it.

The explicit use of structural models allows the relative fractions of the hcp phase (26%) and ccp phase (74%) to be extracted from the refinements in a manner that would be impossible if Pawley fits were used, though some uncertainty remains in these phase fractions due to the overlapping intensity of unindexed peaks with the dominant 111 peak of the ccp Co phase at $2\theta = 12.67°$.

3.3.2 SEM and TEM characterization

SEM micrographs (Figure 3a) show large micron sized particles of NWs. Higher magnification (Figure 3b) shows the NWs are long (>200nm), flexible and homogenous; they

appear to grow from the surface of the particle outwards and are very well intermixed. To obtain further information on the phases present and the direction of growth, the NWs are also characterized using TEM (Figure 3.4). Co NWs reported previously tend to be made of single crystal hcp Co growing continuously in the 002 direction,[5,32,33] however this new morphology shows an unassisted growth mechanism that produces curved, flexible NWs.

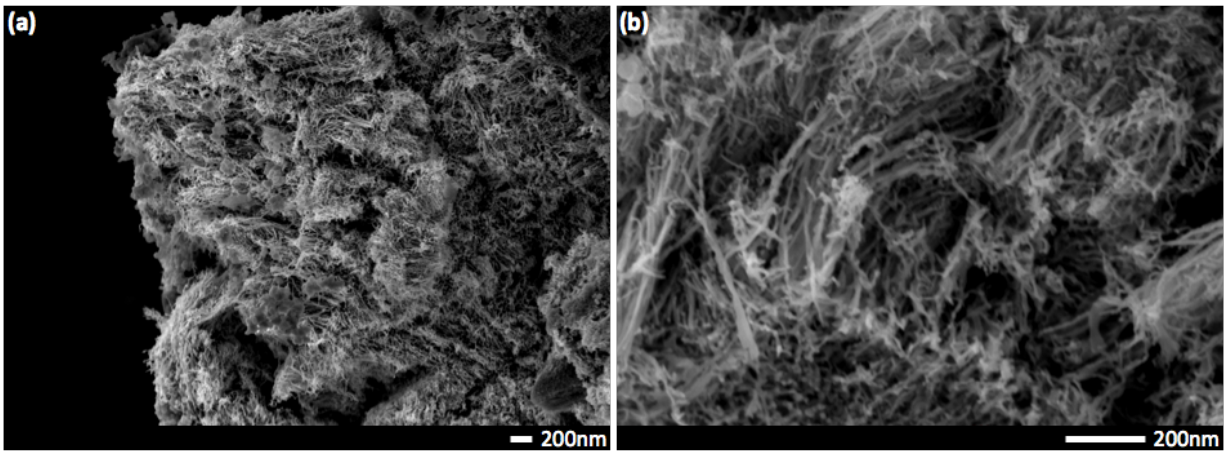

Figure 3.3: SEM micrographs showing micron sized particles of Co NWs (a, b). Higher magnification (b) shows flexible, homogenous wires of ~10 nm diameter. Scale bars are 200nm.

TEM images of the Co NWs show multi-crystalline regions of intersecting phases. Image analysis using ImageJ of the higher resolution images combined with the SEM images show the NWs have a high aspect ratio (~11 nm diameter and ~276 nm long, Supporting Information S5). Selected area electron diffraction (SAED) micrographs show lattice spacings of 2.02 Å corresponding to that of (002) direction of hcp phase cobalt (Figure 3.4) as well as an instance of 2.16 Å corresponding to the (100) direction (Figure 3.4c). This corresponds well with previous reports of Co NWs synthesized by a polyol process where cobalt nanorods are obtained by reduction of carboxylate Co^{II} salts in which the dominant direction is (002).[5,32] Growth in this direction is likely due to a thermodynamic driving force to minimize the total surface free energy by exposing lower surface free energy facets and therefore growing along the higher energy (002)

facet.[34] Other regions also show the ccp phase is present with lattice spacings of 2.05 Å corresponding to the (111) facet (Supporting Information S6). These observations are consistent with the results from the XRD analysis. An intersection of these phases shows that the wires do not grow continuously in one direction but are rather a multigrain product which contributes to their flexible morphology. This most closely resembles a coalescence attachment growth in which nanoparticles serve as building blocks to form winding polycrystalline chains.[35,36] We note that the phase fractions derived from synchrotron XRD fittings differ slightly from TEM observations because larger hcp domains are easier to resolve than small ccp domains and TEM is a local probe not meant for quantifying average behavior.

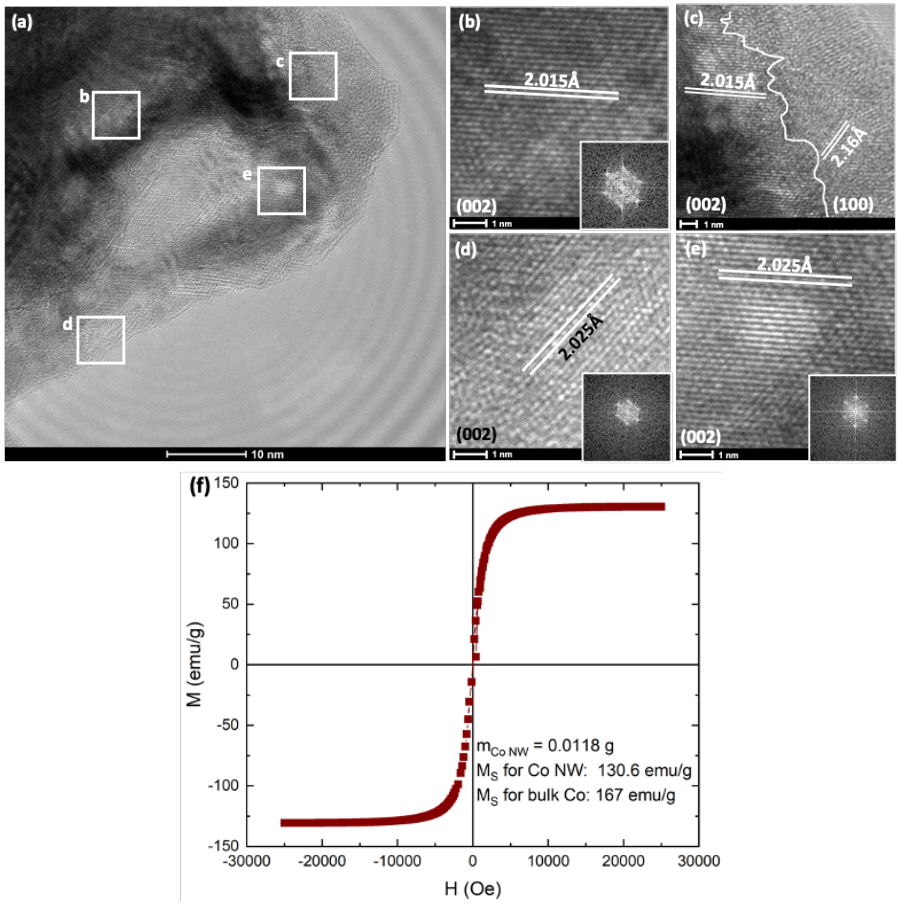

Figure 3.4: TEM micrographs of Co NWs (a) with SAED insets of regions showing predominantly hcp phase (b, c, d, e) as well as the intersection of grains (c). Magnetic measurements show the M_s of NWs is close to the value of bulk cobalt value (f).

The magnetic properties of the Co NWs are measured using vibrating sample magnetometry (Figure 4f). The saturation magnetization (M_s) is found to be 130.6 emu/g, achieving 78% the value of bulk cobalt. Such a high magnetization exceeds recorded values previously reported for cobalt nanoparticles and nanorods (102 and 113 emu/g respectively).[5,37] Co is known to be a ferromagnetic material and is often used in hard magnets to raise the Curie temperature and improve magnetic properties due to an enhanced interdiffusion across interfaces.[37,38] The NWs' strong magnetic properties combined with their curved morphology make them a promising candidate for applications such as spintronic circuits and magnetic sensors.[6,7] Additionally, intergrowths and stacking faults in the cobalt nanoparticle catalysts have shown high catalytic activities in the Fischer-Tropsch synthesis.[4] It is helpful to note that grain size also affects magnetic properties with work showing that smaller grain size leads to reduced connectivity, resulting in higher total resistivity.[39,40] Doping the NWs can also lead to phase transitions which can affect whether the material is in a weak ferromagnetic state or in a mixture of antiferromagnetic and magnetic states.[41,42] Future work for enhancing electronic properties can investigate the addition of a second phase which can significantly improve the dielectric properties of the NWs.[43,44]

3.3.3 Comparison with similar systems

Based on these observations, we hypothesize that the anisotropic hcp phase in a dilute precursor is what results in NW formation and next examine its validity by using other related precursors. Li_2CoCl_4, which has an orthorhombic crystal structure and is a less dilute system than Li_6CoCl_8, can be used to probe whether the dilution or crystal structure of the precursor plays a more dominant role in the formation mechanism of NWs. Li_2CoCl_4 was synthesized according to

report by Kanno et al[21] and XRD results show the formation of the Li_2CoCl_4 phase as well as the conversion to the nanocomposite of LiCl and Co (Supporting Information S7). SEM images show the same flexible, thin and long NWs as those produced from the Suzuki phase precursor (Figure 3.5b). These contrast with a nanoporous metal morphology when $CoCl_2$ was used as a precursor (Figure 3.5c).[19] While the exact mechanism is unclear, the comparison of various dilutions of the precursor metal halide from $CoCl_2$ to Li_2CoCl_4 to Li_6CoCl_8 shows that dilution is necessary to produce NWs. This may be because of a combination of small volume change and an extrusion-like process during lithiation. The formation of NWs from a less dilute precursor as Li_2CoCl_4 also aids in a more efficient synthesis procedure since less LiCl is required and shows that the crystal structure of the precursor is not as important as the dilution of Co in the LiCl matrix.

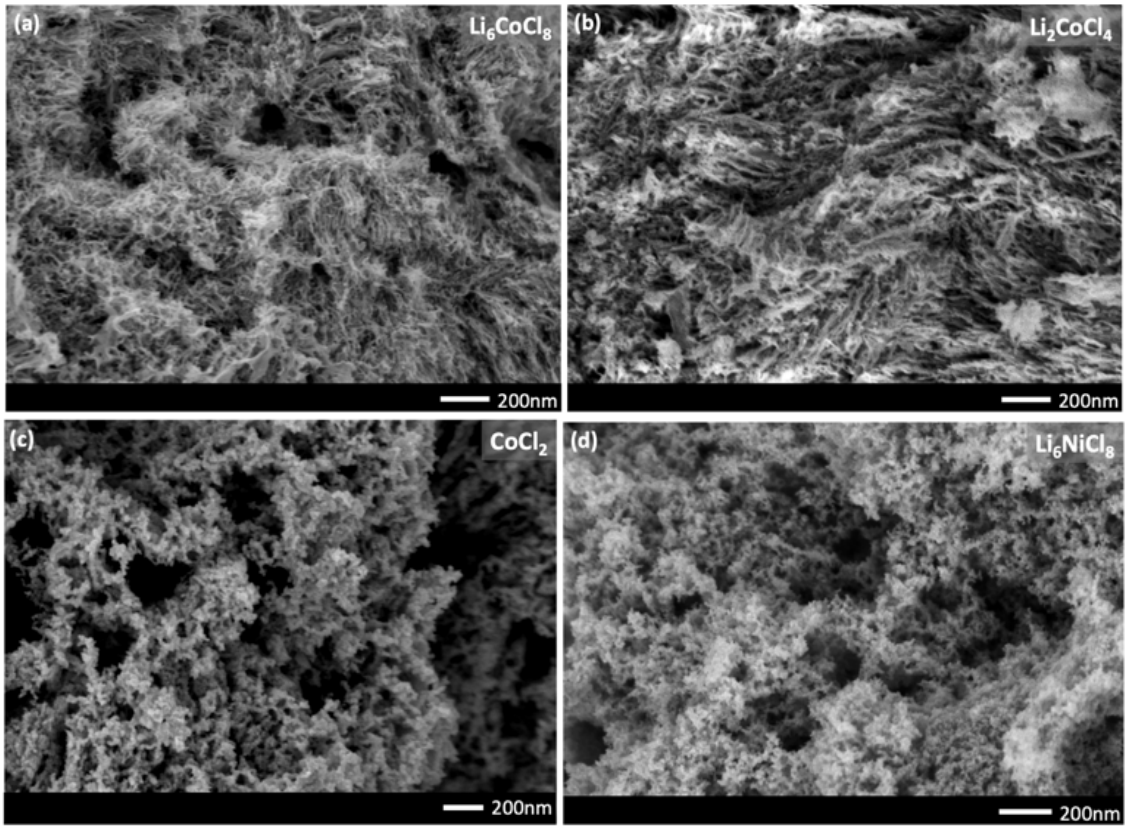

Figure 3.5: SEM images comparing the effect of different precursors: Li_6CoCl_8 and Li_2CoCl_4 produce NWs (a, b), however less dilution (c, $CoCl_2$) and a different ccp metal (d, Li_6NiCl_8) lead to nanoporous morphology.

Additionally, Li_6NiCl_8 was synthesized to isolate the effect of a dilute salt matrix by keeping the same metal to LiCl ratio as the Li_6CoCl_8 precursor but using a different transition metal that does not have an anisotropic phase. The XRD pattern shows the Suzuki peaks in the Ni system, as well as conversion to the nanocomposite and the final product (Supporting Information S8). SEM images of the final product, however, reveal a nanoporous morphology similar to that derived from previously reported $NiCl_2$ precursors (Figure 3.5d).[19] This result suggests that a critical parameter for forming NWs is the anisotropic hcp phase that leads to NWs due to the lower energy barrier of growing in a preferential direction. Since Ni is only present in the fcc phase, there is no driving force to produce anisotropic morphology.

Several key parameters that help achieve 1D growth in metal NWs are highlighted: 1) a precursor with a low metal concentration experiences a small volume change during lithiation and encourages a slow, extrusion type of phase conversion process; the resultant small size leads to a mixture of hcp vs ccp phases, 2) the precursor metal must be able to exist in an anisotropic phase which allows growth in a preferred orientation. Additionally, the mixture of both Co phases with the larger hcp phase being smaller than the NW dimensions and possible stacking faults due to a coalescence attachment growth mechanism may contribute to the curved morphology.[35,45]

3.4 Conclusions

This work presents a novel method of synthesizing cobalt nanowires from bulk precursors without the addition of catalysts or external stimuli. By using a dilute Suzuki phase precursor, Li_6CoCl_8, reacting with *n*-butyllithium to create a nanocomposite, and then dissolving the resulting salt, a cobalt nanowire morphology is achieved. This is enabled by both the dilute salt matrix which affects the cobalt crystallite size as well as the significant presence of the hcp phase. Ultimately,

the anisotropic hcp phase allows for preferred growth in the (002) direction. The same NW morphology can be achieved with a less dilute precursor such as Li_2CoCl_4, however using a ccp metal such as Ni in Li_6NiCl_8 results in a nanoporous morphology. A high saturation magnetization value of 130.6 emu/g shows the Co NW's magnetic properties exceed those of previously reported cobalt nanoparticles and nanorods; a property important for applications such as flexible electronics, magnetic sensors and catalysts.[5–7,37] This work provides a scalable synthesis procedure at ambient conditions that can help pave the way for future designs of nanowires.

3.5 Acknowledgments

Chapter 3, in full, is a reprint of the material as it appears in RSC Advances, V. Petrova, A. A. Corrao, S. Wang, Y. Xiao, K. W. Chapman, E. E. Fullerton, P. G. Khalifah and P. Liu. 2022. The dissertation author was the primary researcher and author of this paper.

SUPPLEMENTAL INFORMATION

1. Time dependence

It is found that full conversion of Li_6CoCl_8 to Co/LiCl takes place on the order of weeks (Fig S1a). While full conversion can be seen after 30 days, partial conversion still allows for the formation of NWs since the residual precursor is soluble and washed away in the methanol rinse. NWs can be formed using both fully and partially converted nanocomposites as shown in the SEM image from a 30 day converted nanocomposite (Fig S1b).

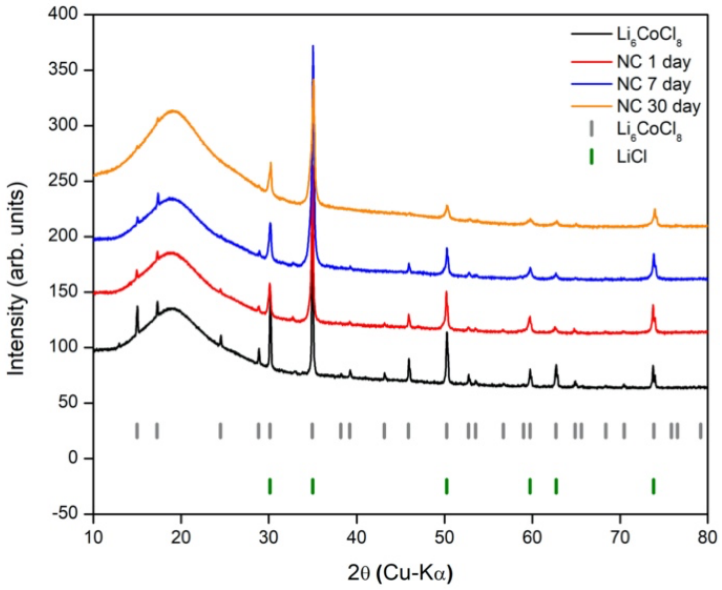

Figure 3.6: Laboratory X-ray diffraction data of nanocomposites resulting from reduction of Li_6CoCl_8 after 1 (red), 7 (blue) and 30 (orange) days of reaction.

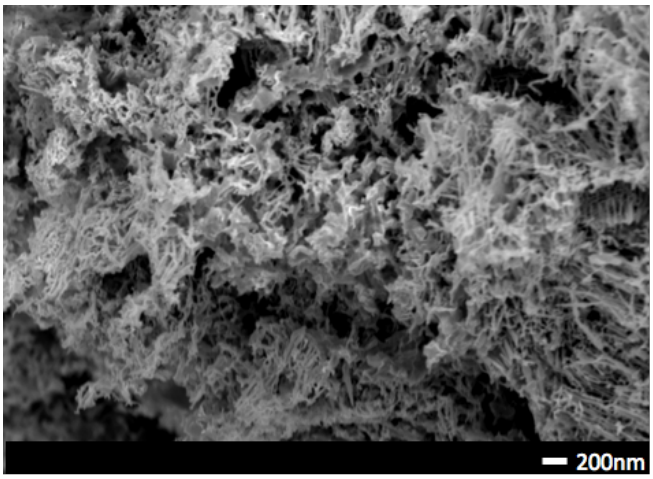

Figure 3.7: SEM micrograph of Co NWs formed from a 30 day full conversion reaction.

2. Lab-scale XRD of Co NWs

Lab scale XRD is found to be insufficient to characterize Co NWs since it only shows a broad amorphous Co peak. Synchrotron XRD provides a significantly higher signal:noise ratio and is needed to resolve the extremely small nanoscale Co domains as well as the polymorphism and anisotropy of the Co peaks.

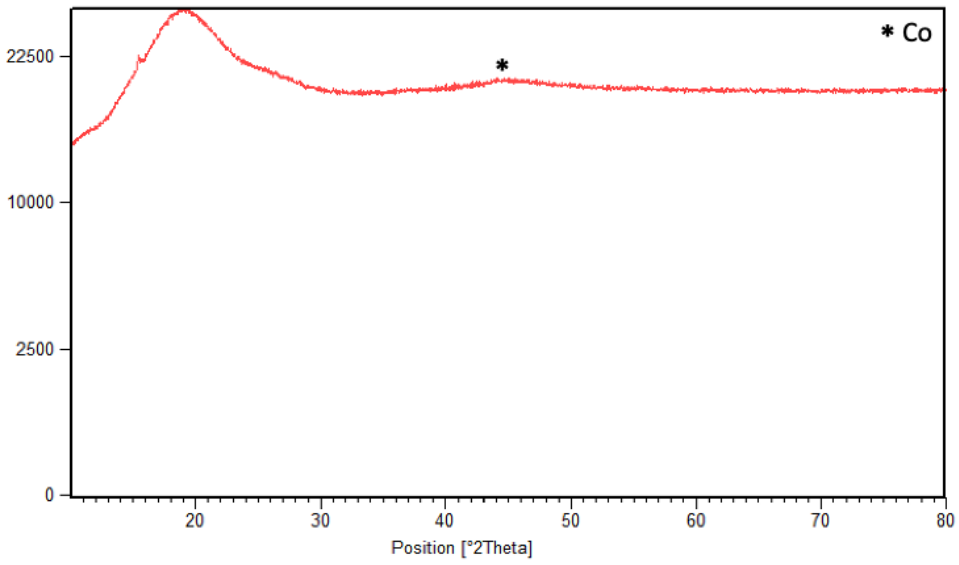

Figure 3.8: Lab-scale XRD of Co NWs features only a broad amorphous peak at ~46 degrees. The broad beak at 20 degrees is due to Kapton covering the sample.

3. XRD results and Rietveld refinement analysis

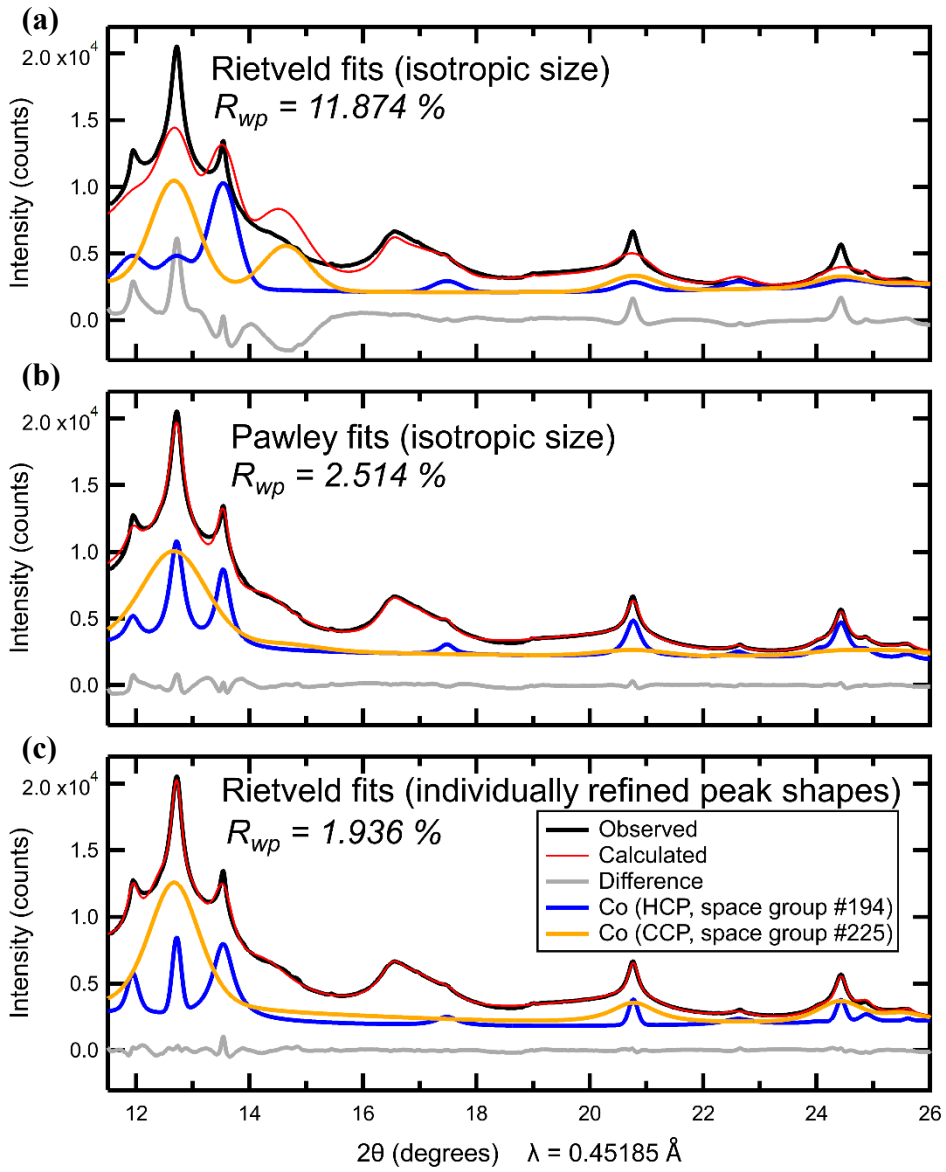

Figure 3.9: Comparison of whole-pattern fits to the Co nanowire sample using (a) Rietveld refinements with an isotropic size model, (b) Pawley methods with an isotropic size model, and (c) our novel Rietveld approach using separately refined peak shapes for each diffraction. The larger breadths of the CCP phase are indicative of a smaller primary particle size than for the CCP phase, consistent with the approximate sizes of 5 nm and 1.6 nm estimated through fits to isotropic size models. Although models combining isotropic size and isotropic strain broadening were considered for Pawley and Rietveld fits, they did not significantly improve the model relative to size-only fits (differed in 3rd decimal of R_{wp}) and thus are not reported.

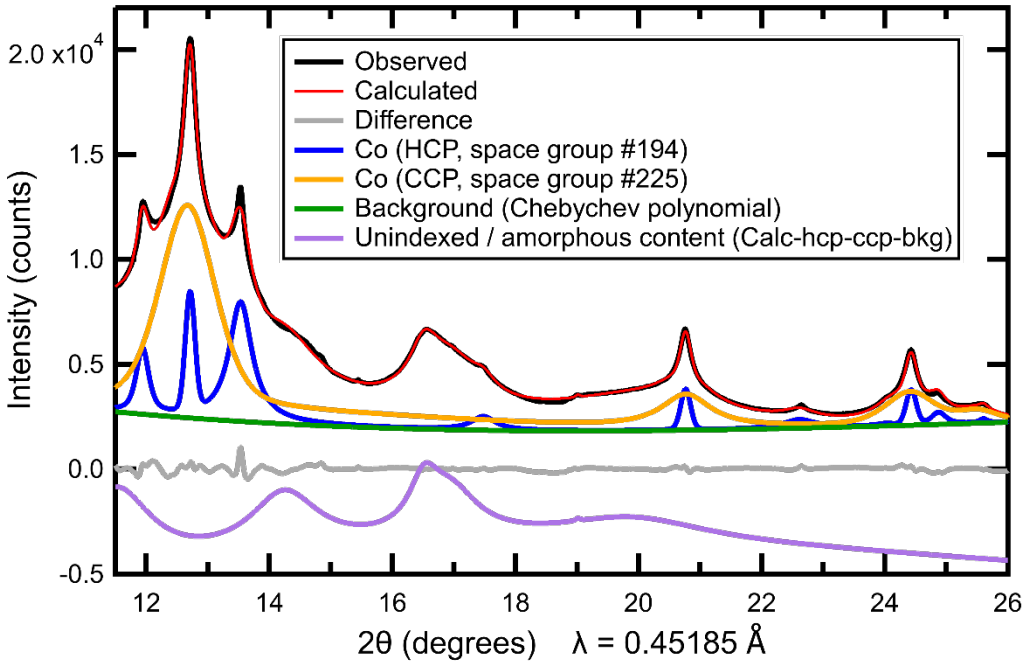

Figure 3.10: Contribution of unindexed diffraction peaks (purple) and the overall background (green) to fits of the Co nanowire sample using novel Rietveld refinements with freely refined peak shapes. The unindexed peaks are comparable in width to those of the CCP Co phase, suggesting a similar domain size (1 – 2 nm) that may indicate their origin as a decomposition layer on the surface of Co.

Table 3.1: Co nanowire peak indexing, positions, and profile parameters from XRD refinements using novel Rietveld refinements with freely refined peak shapes.

Phase	*hkl*	Position (2θ)	*d*-spacing (Å)	Gaussian FWHM	Lorentzian FWHM	Gaussian size	Lorentzian size	Volume-weighted crystallite size (nm)
HCP Co	1 0 0	11.947	2.170	0.124(6)	0.157(5)	20.94	16.51	8.1(2)
(*P6₃/mmc*)	0 0 2	12.721	2.039	0.169(3)	0.000(4)	15.40		14.5(1)
	1 0 1	13.541	1.916	0.0(9)	0.428(7)		6.06	3.86(2)
	1 0 2	17.486	1.486	0.05(9)	0.44(2)	45.70	6.06	3.8(1)
	2 -1 0	20.769	1.253	0.161(5)	0.016(7)	16.33	158.90	13.9(5)
	1 0 3	22.615	1.152	0.08(4)	0.56(2)	33.51	4.63	2.9(1)
	2 0 0	24.027	1.085	0.15(13)	0.25(11)	17.65	10.41	6(2)
	2 -1 2	24.430	1.067	0.167(6)	0.00(1)	15.89		14.9(1)
	2 0 1	24.876	1.048	0.13(2)	0.20(2)	21.21	13.02	6.9(5)
	0 0 4	25.603	1.019	0.09(3)	0.07(3)	27.83	36.52	14(4)
CCP Co	1 1 1	12.679	2.046	0.87(1)	0.34(2)	2.99	7.63	2.01(1)
(*Fm-3m*)	2 0 0	14.650	1.772	6.07(9)	2.4(3)	0.43	1.08	0.29(1)
	2 2 0	20.775	1.253	0.27(3)	0.82(1)	9.75	3.17	1.89(3)
	3 1 1	24.412	1.068	0.67(2)	0.35(3)	3.95	7.44	2.39(5)
	2 2 2	25.516	1.023	0.499(9)	0.32(1)	5.32	8.14	2.96(6)

The Co nanowire sample consisted of a two-phase mixture of two different Co polymorphs, HCP and CCP. The HCP Co phase was refined in space group *P6₃/mmc* (#194) with lattice parameters of $a = 2.50675(6)$ and $c = 4.0788(1)$, with a single crystallographic site at the 2c Wykoff position of $x = 1/3$, $y = 2/3$, and $z = 1/4$.[1] The CCP Co phase was refined in space group *Fm-3m* (#225) with lattice parameters of $a = 3.5441(2)$, with a single crystallographic site at the 4a Wykoff position of $x = 0$, $y = 0$, $z = 0$. The Co B-value was constrained to be the same in the HCP and CCP phases and refined to a value of 3.11(7). The refined volume fractions were 26% HCP and 74% CCP.

Gaussian and Lorentzian size parameters (not to be interpreted as an actual size) are calculated as follows from the G and L contributions to full width at half maximum refined for each *hkl* peak:

$$Size = \frac{\left(\frac{180}{\pi}\right)\lambda}{cos(\theta)} \cdot \frac{1}{fwhm(2\theta)}$$

Volume-weighted crystallite sizes are physically meaningful crystallite sizes based on volume-weighted column lengths determined through an integral breadth method. This approach is approximately independent of the shape factor (K = 1) which affects the calculated crystallite size in the Scherrer equation since knowledge of the particle shape and size distribution is typically not known. The volume-weighted size (L_{vol} in units of nm) is calculated as shown in the equation below, where β_{IB} is defined as the width of a rectangle with the same height and area as the line profile, obtained from dividing the line profile area by the line profile height.[2]

$$L_{vol} = \frac{\lambda}{\beta_{IB} \cdot cos\theta}$$

Instrument and source contribution to peak profiles were described using a 6-term pseudo-Voigt function with parameters determined from a refinement using a diffraction pattern collected on NIST LaB_6 standard reference material loaded in an equivalent manner to the samples.

fwhm = ha + hb tanθ + hc/cosθ (full width at half maximum)

η = lora + lorb tanθ + lorc/cosθ (Lorentzian/Gaussian mixing parameter)

ha = 0.02609478, hb = 0.04675279, hc = 0.02605727

lora = 0.08689309, lorb = 0.0100875, lorc = 0.02393109

Table 3.2: Position, d-spacing, intensity, and size (nm) for unindexed / amorphous content fit with individual peaks from XRD refinements.

Position (2θ)	*d*-spacing (Å)	Intensity (counts)	Volume-weighted crystallite size (nm)
11.5	2.25501	98(3)	1.23(3)
14.249	1.82159	85(3)	1.31(2)
16.521	1.57248	40(2)	2.87(7)
16.95	1.53296	91(3)	1.41(2)
19.02	1.36742	1.0(1)	1.0(1)
19.9	1.30752	179(6)	0.56(1)

Table 3.3: Co nanowire peak profile parameters from XRD refinements using conventional isotropic size broadening in Rietveld and Pawley methods.

Refinement method	Phase	Gaussian size	Lorentzian size	Volume-weighted crystallite size (nm)
Rietveld (isotropic size)	HCP Co (*$P6_3/mmc$*)	4.5(2)	N/A	4.2(4)
Rietveld (isotropic size)	CCP Co (*Fm-3m*)	2.8(1)	N/A	2.6(2)
Pawley (isotropic size)	HCP Co (*$P6_3/mmc$*)	N/A	9.1(1)	5(1)
Pawley (isotropic size)	CCP Co (*Fm-3m*)	1.69(2)	8.9(5)	1.63(2)

Size parameters are reported as N/A when their contributions to the peak width are negligible

4. Dimensions of Co NWs using ImageJ image analysis

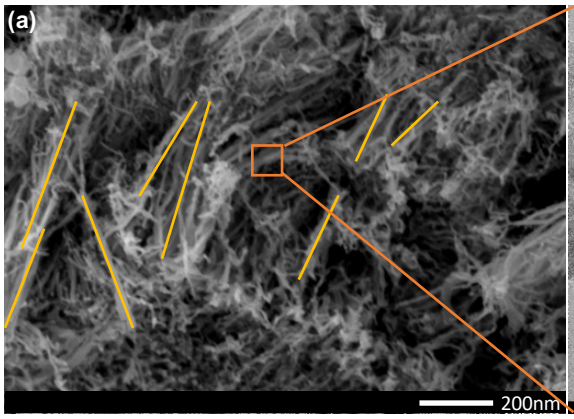

	Length (nm)	Diameter (nm)
1	326.5	11.5
2	208.2	9.7
3	391.9	11.2
4	286.5	11.8
5	378.7	13.5
6	238.5	11.5
7	197.7	9.8
8	180.2	
Avg	**276**	**11.3**

Figure 3.11: Analysis using ImageJ of SEM images showing an average length of 276 nm (7 data points) and higher resolution TEM images showing an average diameter of 11.3 nm (8 data points).

5. Additional TEM on Co NWs showing CCP phase

While the growth of Co NWs is predominately in the (002) direction of hcp phase cobalt, the ccp phase is also present in the product with lattice spacings of 2.05Å corresponding to the (111) facet.

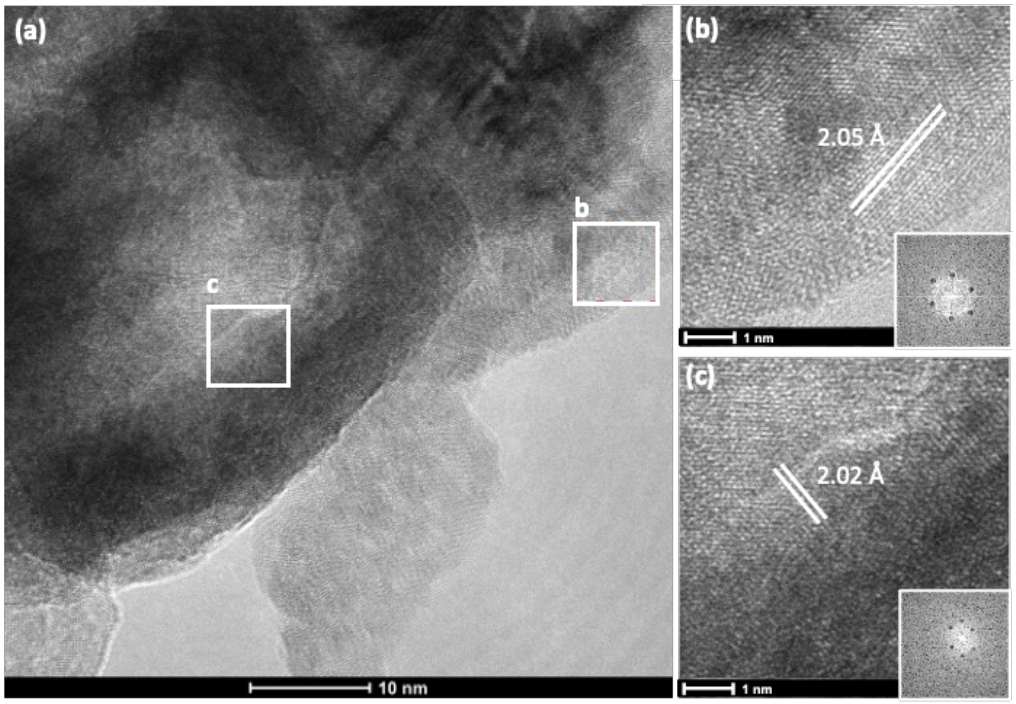

Figure 3.12: TEM micrographs of Co NWs (a) with an SAED insets of region showing CCP phase of Co with 2.05Å lattice spacings (b) and HCP phase with 2.02Å (c).

6. Li_2CoCl_4

Li_2CoCl_4 was synthesized in the same manner as Li_6CoCl_8, however with the appropriate $LiCl:CoCl_2$ stoichiometry and heated at 315°C based on the phase diagram.

Li_2CoCl_4 also shows that a dilute precursor with Co can form NWs. XRD results show the formation of the Li_2CoCl_4 phase, the converted nanocomposite and final Co product. The final NW product does not show any sharp peaks due to the small crystallite size of Co and the limitations of the benchtop XRD.

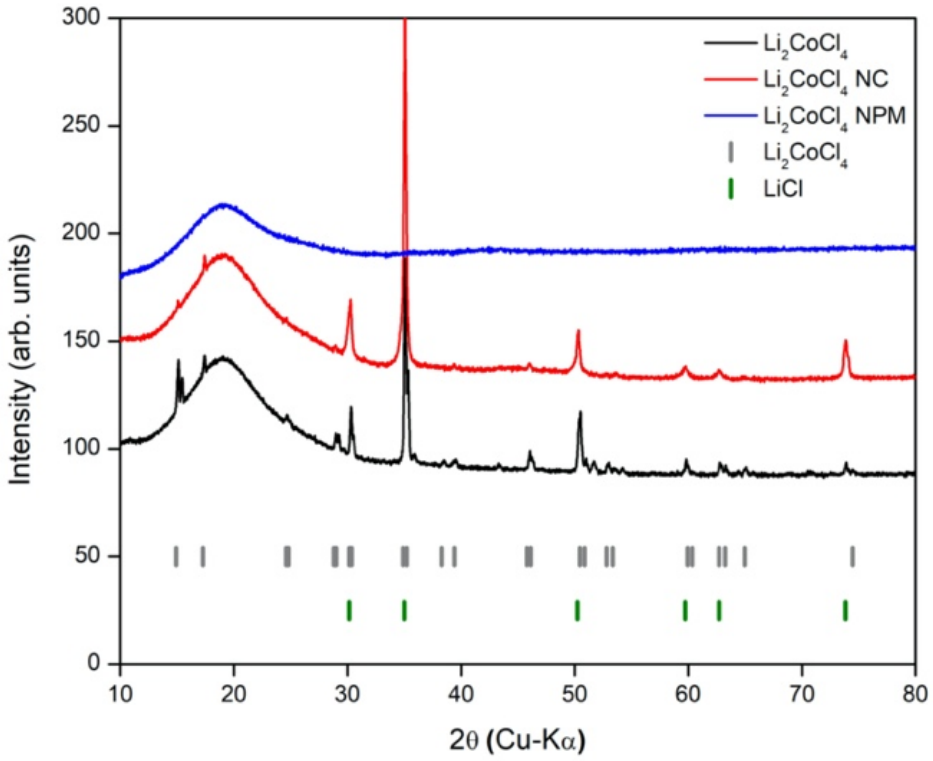

Figure 3.13: Laboratory X-ray diffraction data of Li_2CoCl_4 and the resulting nanocomposite from reduction. Tick marks for *hkl*s of orthorhombic Li_2CoCl_4 (gray) and rocksalt-type LiCl (green) are labeled.

7. Li_6NiCl_8

Li_6NiCl_8 was synthesized in the same manner as Li_6CoCl_8 but with $NiCl_2$ (98% Sigma-Aldrich) instead of $CoCl_2$ and heated at 540°C for 1 week based on its phase diagram. Li_6NiCl_8 is known to phase separate back to $NiCl_2$ and LiCl when cooled slowly, so the ampoule was rapidly taken from the furnace and air-quenched to room temperature before being stored in an argon glovebox. Li_6NiCl_8 shows that a dilute precursor with Ni does not form NWs. XRD results show the formation of the Li_6NiCl_8 phase, the converted nanocomposite and final Ni product.

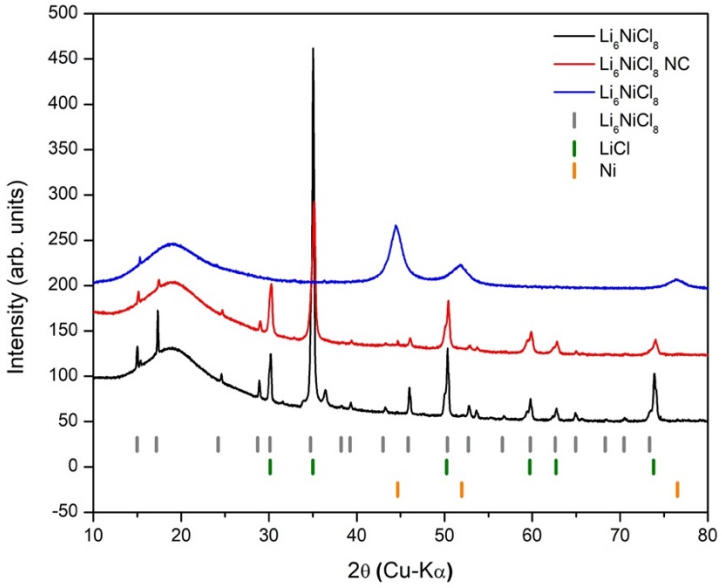

Figure 3.14: Laboratory X-ray diffraction data of Li_6NiCl_8 and the resulting nanocomposite from reduction. Tick marks for *hkl*s of Li_6NiCl_8 (gray), rocksalt-type LiCl (green) and FCC Ni (orange) are labeled.

Supplemental Information References

(1) Fujihisa, H.; Takemura, K. Equation of State of Cobalt up to 79 GPa. *Physical Review B - Condensed Matter and Materials Physics* **1996**, *54* (1), 5–7. https://doi.org/10.1103/PhysRevB.54.5.

(2) Patterson, A. L. The Scherrer Formula for X-Ray Particle Size Determination. *Physical Review* **1939**, *56* (10), 978–982. https://doi.org/10.1103/PhysRev.56.978.

REFERENCES

(1) Chen, L.; Liu, Y.; Zhao, Y.; -, al. One-Dimensional Nanomaterials for Energy Storage Related Content Graphene Based 2D-Materials for Supercapacitors Thangavelu Palaniselvam and Jong-Beom Baek-Graphene-Based Fibers for Supercapacitor Applications. *Journal of Physics D: Applied Physics* **2018**, *51*, 113002.

(2) Huo, D.; Kim, M. J.; Lyu, Z.; Shi, Y.; Wiley, B. J.; Xia, Y. One-Dimensional Metal Nanostructures: From Colloidal Syntheses to Applications. *Chemical Reviews* **2019**, *119* (15), 8972–9073.

(3) Gandha, K.; Elkins, K.; Poudyal, N.; Liu, X.; Liu, & J. P. High Energy Product Developed from Cobalt Nanowires. *Nature Scientific Reports* **2014**.

(4) Price, S. W. T.; Martin, D. J.; Parsons, A. D.; Sławiński, W. A.; Vamvakeros, A.; Keylock, S. J.; Beale, A. M.; Mosselmans, J. F. W. Chemical Imaging of Fischer-Tropsch Catalysts under Operating Conditions. *Science Advances* **2017**, *3* (3).

(5) Soumare, Y.; Garcia, C.; Maurer, T.; Chaboussant, G.; Ott, F.; Fiévet, F.; Piquemal, J.; Viau, G. Kinetically Controlled Synthesis of Hexagonally Close-Packed Cobalt Nanorods with High Magnetic Coercivity. *Advanced Functional Materials* **2009**, *19* (12), 1971–1977.

(6) Muscas, G.; Jönsson, P. E.; Serrano, I. G.; Vallin, Ö.; Kamalakar, M. V. Ultralow Magnetostrictive Flexible Ferromagnetic Nanowires. *Nanoscale* **2021**, *13* (12), 6043–6052.

(7) Ota, S.; Ando, A.; Chiba, D. A Flexible Giant Magnetoresistive Device for Sensing Strain Direction. *Nature Electronics* **2018**, *1* (2), 124–129.

(8) Trukhanov, A. v.; Turchenko, V. O.; Bobrikov, I. A.; Trukhanov, S. v.; Kazakevich, I. S.; Balagurov, A. M. Crystal Structure and Magnetic Properties of the BaFe12-XAlxO19 (X=0.1-1.2) Solid Solutions. *Journal of Magnetism and Magnetic Materials* **2015**, *393*, 253–259.

(9) Trukhanov, A. v.; Trukhanov, S. v.; Panina, L. v.; Kostishyn, V. G.; Chitanov, D. N.; Kazakevich, I. S.; Trukhanov, A. v.; Turchenko, V. A.; Salem, M. M. Strong Corelation between Magnetic and Electrical Subsystems in Diamagnetically Substituted Hexaferrites Ceramics. *Ceramics International* **2017**, *43* (7), 5635–5641.

(10) Trukhanov, A. v.; Grabchikov, S. S.; Sharko, S. A.; Trukhanov, S. v.; Trukhanova, K. L.; Volkova, O. S.; Shakin, A. Magnetotransport Properties and Calculation of the Stability of GMR Coefficients in CoNi/Cu Multilayer Quasi-One-Dimensional Structures. *Materials Research Express* **2016**, *3* (6).

(11) Sharko, S. A.; Serokurova, A. I.; Zubar, T. I.; Trukhanov, S. v.; Tishkevich, D. I.; Samokhvalov, A. A.; Kozlovskiy, A. L.; Zdorovets, M. v.; Panina, L. v.; Fedosyuk, V. M.; Trukhanov, A. v. Multilayer Spin-Valve CoFeP/Cu Nanowires with Giant Magnetoresistance. *Journal of Alloys and Compounds* **2020**, *846*, 156474.

(12) Wen, L.; Xu, R.; Mi, Y.; Lei, Y. Multiple Nanostructures Based on Anodized Aluminium Oxide Templates. *Nature Nanotechnology* **2017**, *12* (3), 244–250.

(13) Wang, N.; Cai, Y.; Zhang, R. Q. Growth of Nanowires. *Materials Science and Engineering R: Reports*. 2008.

(14) Thakur, A.; Sharma, N.; Bhatti, M.; Sharma, M.; Trukhanov, A. v.; Trukhanov, S. v.; Panina, L. v.; Astapovich, K. A.; Thakur, P. Synthesis of Barium Ferrite Nanoparticles Using Rhizome Extract of Acorus Calamus: Characterization and Its Efficacy against Different Plant Phytopathogenic Fungi. *Nano-Structures and Nano-Objects* **2020**, *24*, 100599.

(15) Algarou, N. A.; Slimani, Y.; Almessiere, M. A.; Alahmari, F. S.; Vakhitov, M. G.; Klygach, D. S.; Trukhanov, S. v.; Trukhanov, A. v.; Baykal, A. Magnetic and Microwave Properties of SrFe12O19/MCe0.04Fe1.96O4 (M = Cu, Ni, Mn, Co and Zn) Hard/Soft Nanocomposites. *Journal of Materials Research and Technology* **2020**, *9* (3), 5858–5870.

(16) Xia, Y.; Yang, P.; Sun, Y.; Wu, Y.; Mayers, B.; Gates, B.; Yin, Y.; Kim, F.; Yan, H. One-Dimensional Nanostructures: Synthesis, Characterization, and Applications. *Advanced Materials*. John Wiley & Sons, Ltd March 4, 2003, pp 353–389.

(17) Lei, D.; Benson, J.; Magasinski, A.; Berdichevsky, G.; Yushin, G. Transformation of Bulk Alloys to Oxide Nanowires. *Science (1979)* **2017**, *355* (6322), 267–271.

(18) Wang, F.; Turcheniuk, K.; Wang, B.; Song, A.-Y.; Ren, X.; Vallamattam, A.; Park, A.; Hanley, K.; Zhu, T.; Yushin, G. Mechanisms of Transformation of Bulk Aluminum−Lithium Alloys to Aluminum Metal−Organic Nanowires. **2018**.

(19) Coaty, C.; Zhou, H.; Liu, H.; Liu, P. A Scalable Synthesis Pathway to Nanoporous Metal Structures. *ACS Nano* **2018**, *12* (1), 432–440.

(20) Kanno, R.; Takeda, Y.; Takahashi, A.; Yamamoto, O.; Suyama, R.; Koizumi, M. New Double Chloride in the LiCl-CoCl2 System: I. Preparation, Crystal Structure, Phase Transformation, and Ionic Conductivity of Li6CoCl8. *Journal of Solid State Chemistry* **1987**, *71* (1), 189–195.

(21) Kanno, R.; Takeda, Y.; Takahashi, A.; Yamamoto, O.; Suyama, R.; Kume, S. New Double Chloride in the LiCl-CoCl2 System: II. Preparation, Crystal Structure, Phase Transformation, and Ionic Conductivity of Li2CoCl4 Spinel. *Journal of Solid State Chemistry* **1987**, *71* (1), 196–204.

(22) Lutz, H. D.; Kuske, P.; Wussow, K. Neue Lithiumchlorid-Suzukiphasen: Li6MCl8(M = Fe, Co, Ni). *Zeitschrift für anorganische und allgemeine Chemie* **1987**, *553* (10), 172–178.

(23) Kononova, O.; Huo, H.; He, T.; Rong, Z.; Botari, T.; Sun, W.; Tshitoyan, V.; Ceder, G. Text-Mined Dataset of Inorganic Materials Synthesis Recipes. *Scientific Data* **2019**, *6* (1), 1–11.

(24) Hua, X.; Eggeman, A. S.; Castillo-martínez, E.; Robert, R.; Geddes, H. S.; Lu, Z.; Pickard, C. J.; Meng, W.; Wiaderek, K. M.; Pereira, N.; Amatucci, G. G.; Midgley, P. A.; Chapman, K. W.;

Steiner, U.; Goodwin, A. L.; Grey, C. P. Revisiting Metal Fluorides as Lithium-Ion Battery Cathodes. *Nature Materials* **2021**.

(25) Coaty, C. M.; Corrao, A. A.; Petrova, V.; Kim, T.; Fenning, D. P.; Khalifah, P. G.; Liu, P. Anisotropic Nanoporous Morphology of ZnO-Supported Co That Enhances Catalytic Activity. *Nanoscale* **2021**, *13* (17), 8242–8253.

(26) Dehghan, R.; Hansen, T. W.; Wagner, J. B.; Holmen, A.; Rytter, E.; Borg, Ø.; Walmsley, J. C. In-Situ Reduction of Promoted Cobalt Oxide Supported on Alumina by Environmental Transmission Electron Microscopy. *Catalysis Letters* **2011**, *141* (6), 754–761.

(27) Sławiński, W. A.; Zacharaki, E.; Fjellvåg, H.; Sjåstad, A. O. Structural Arrangement in Close-Packed Cobalt Polytypes. *Crystal Growth and Design* **2018**, *18* (4), 2316–2325.

(28) Kitakami, O.; Sato, H.; Shimada, Y.; Sato, F.; Tanaka, M. Size Effect on the Crystal Phase of Cobalt Fine Particles. *Physical Review B - Condensed Matter and Materials Physics* **1997**, *56* (21), 13849–13854.

(29) Stephens, P. W. Phenomenological Model of Anisotropic Peak Broadening in Powder Diffraction. *Journal of Applied Crystallography* **1999**, *32* (2), 281–289.

(30) Ectors, D.; Goetz-Neunhoeffer, F.; Neubauer, J. Domain Size Anisotropy in the Double-Voigt Approach: An Extended Model. *Journal of Applied Crystallography* **2015**, *48* (6), 1998–2001.

(31) Ectors, D.; Goetz-Neunhoeffer, F.; Neubauer, J. A Generalized Geometric Approach to Anisotropic Peak Broadening Due to Domain Morphology. *Journal of Applied Crystallography* **2015**, *48* (1), 189–194.

(32) Ciuculescu, D.; Ed, F.; Dumestre, E.; Comesa~ Na-Hermo, M.; Chaudret, B.; Spasova, M.; Farle, M.; Amiens, C. Single-Crystalline Co Nanowires: Synthesis, Thermal Stability, and Carbon Coating. *Chem. Mater* **2009**, *21*, 3987–3995.

(33) Maaz, K.; Karim, • S; Usman, • M; Mumtaz, • A; Liu, • J; Duan, J. L.; Maqbool, • M. Effect of Crystallographic Texture on Magnetic Characteristics of Cobalt Nanowires. *Nanoscale* **2010**, *5*, 1111–1117.

(34) Xia, Y.; Xia, X.; Peng, H. C. Shape-Controlled Synthesis of Colloidal Metal Nanocrystals: Thermodynamic versus Kinetic Products. *J Am Chem Soc* **2015**, *137* (25), 7947–7966.

(35) Liao, H. G.; Cui, L.; Whitelam, S.; Zheng, H. Real-Time Imaging of Pt3Fe Nanorod Growth in Solution. *Science (1979)* **2012**, *336* (6084), 1011–1014.

(36) Thanh, N. T. K.; Maclean, N.; Mahiddine, S. Mechanisms of Nucleation and Growth of Nanoparticles in Solution. *Chemical Reviews* **2014**, *114* (15), 7610–7630.

(37) Chaudhary, V.; Zhong, Y.; Parmar, H.; Sharma, V.; Tan, X.; Ramanujan, R. v. Mechanochemical Synthesis of Iron and Cobalt Magnetic Metal Nanoparticles and Iron/Calcium Oxide and Cobalt/Calcium Oxide Nanocomposites. *ChemistryOpen* **2018**, *7* (8), 590–598.

(38) Cullity, B.D. , Graham, C. D. *Introduction to Magnetic Materials*; 2009; Vol. 12.

(39) Trukhanov, S. v.; Troyanchuk, I. O.; Fedotova, V. v.; Ryzhov, V. A.; Maignan, A.; Flahaut, D.; Szymczak, H.; Szymczak, R. Magnetic Properties of the Nonstoichiometric Sr-Doped Manganites. *Physica Status Solidi (B) Basic Research* **2005**, *242* (5), 1123–1131.

(40) Doroshev, V. D.; Borodin, V. A.; Kamenev, V. I.; Mazur, A. S.; Tarasenko, T. N.; Tovstolytkin, A. I.; Trukhanov, S. v. Self-Doped Lanthanum Manganites as a Phase-Separated System: Transformation of Magnetic, Resonance, and Transport Properties with Doping and Hydrostatic Compression. *Journal of Applied Physics* **2008**, *104* (9).

(41) Trukhanov, S. V.; Lobanovski, L. S.; Bushinsky, M. V.; Troyanchuk, I. O.; Szymczak, H. Magnetic Phase Transitions in the Anion-Deficient. *Journal of Physics Condensed Matter* **2003**, *15*, 1783–1795.

(42) Trukhanov, S. v.; Kozlenko, D. P.; Trukhanov, A. v. High Hydrostatic Pressure Effect on Magnetic State of Anion-Deficient La0.70Sr0.30MnOx Perovskite Manganites. *Journal of Magnetism and Magnetic Materials* **2008**, *320* (14), 91–94.

(43) Almessiere, M. A.; Trukhanov, A. v.; Slimani, Y.; You, K. Y.; Trukhanov, S. v.; Trukhanova, E. L.; Esa, F.; Sadaqati, A.; Chaudhary, K.; Zdorovets, M.; Baykal, A. Correlation between Composition and Electrodynamics Properties in Nanocomposites Based on Hard/Soft Ferrimagnetics with Strong Exchange Coupling. *Nanomaterials* **2019**, *9* (2).

(44) Trukhanov, A. v.; Algarou, N. A.; Slimani, Y.; Almessiere, M. A.; Baykal, A.; Tishkevich, D. I.; Vinnik, D. A.; Vakhitov, M. G.; Klygach, D. S.; Silibin, M. v.; Zubar, T. I.; Trukhanov, S. v. Peculiarities of the Microwave Properties of Hard-Soft Functional Composites SrTb0.01Tm0.01Fe11.98O19-AFe2O4(A = Co, Ni, Zn, Cu, or Mn). *RSC Advances* **2020**, *10* (54), 32638–32651.

(45) Ducreux, O.; Rebours, B.; Lynch, J.; Roy-Auberger, M.; Bazin, D. Microstructure of Supported Cobalt Fischer-Tropsch Catalysts The Fischer-Tropsch Process Le Procédé Fischer-Tropsch. *Oil & Gas Science and Technology-Rev. IFP* **2009**, *64* (1), 49–62.

CHAPTER 4: EXPLORING KINETICS BEHIND $FeCl_3$ AND FeF_3 CONVERSION REACTIONS IN ALL SOLID-STATE BATTERIES

4.1 Introduction

Recently, improvements in commercial intercalation-based lithium-ion batteries have allowed them to reach capacities approaching their theoretical limits. In order to continue improving the energy density of lithium-ion batteries, novel cathode materials must be developed. Conversion-type cathode materials are ideal candidates for obtaining higher capacities as the conversion reaction typically involves 2-3 Li ions stored by 1 atom of transition metal.

In this work, we introduce a novel cathode material, $FeCl_3$, and compare the first cycle kinetics with FeF_3. While there has been extensive research on FeF_3 and FeF_2 in liquid cells and more recently, solid-state batteries; $FeCl_3$ has never been explored as a battery material due to its dissolution issues in liquid electrolyte and stability issues with current solid-state electrolytes (SSEs). With recent developments in halide-based SSEs, there is now an opportunity to investigate the effect of the anion (Cl vs F) on the thermodynamics and kinetics of $FeCl_3$ and FeF_3 conversion reactions. Conversion cathode materials suffer from high hysteresis due to the many phase transformations associated with accommodating 2-3 Li atoms and the differing reaction pathways that can occur during lithiation and delithiation.

Two factors that can affect the hysteresis of a reaction are the surface energy and diffusion energy barrier between species. A lower surface energy is related to decreased stability of the compound which can lead to lowering the voltage at which the surface breaks down.[1] Meanwhile, a lower diffusion energy barrier can allow for enhanced Li diffusion across the surface, aiding the conversion reaction during diffusion-limited regimes. Computational work done by Ceder et al on the FeF_3 conversion reaction suggests a scenario in which FeF_3 is lithiated to Li_xFeF_3 through topotactic Li insertion, after which nanoscale Fe precipitates out, limited by Fe's diffusion mobility

and simultaneous accommodation of more Li+ ions.[2] Further in-situ analysis through synchrotron XPD, electron scattering techniques and further density functional theory calculations agree that FeF_3 lithiation and delithiation steps are primarily diffusion-controlled processes limited by the concurrent Li insertion and Fe extrusion.[3]

Indeed the high surface energies and low Li ion diffusion energy barriers of both LiCl and LiF have led to their application as a protective layer on Li metal to create a stable SEI that inhibits interfacial side reactions and allows for long cycle life.[4–7] Counterintuitively, while LiCl and LiF are known to be resistive with low ionic conductivity, it is speculated that their lithium diffusion coefficients makes them ideal candidates for stabilizing CEI and SEI surfaces.[8–10]

$FeCl_3$ and FeF_3 are selected for comparison to better understand the origins of hysteresis commonly found in conversion reactions. $FeCl_3$ and FeF_3 conversion reactions are expected to produce $FeCl_2$ and FeF_2 intermediates on the way to form the final Fe and lithium halide two-phase product (LiCl and LiF respectively). Therefore, the main difference in reaction kinetics between the two systems lies in the difference in interfacial energies between LiCl/Fe and LiF/Fe. While LiF exhibits a slightly higher surface energy than LiCl, it is expected that LiCl's lower diffusion barrier[1] can lead to a lower hysteresis during the conversion reaction.

In this work, we find that $FeCl_3$ exhibits a significantly lower hysteresis during the second plateau (often related to the conversion reaction) than FeF3 resulting in overall higher stability during cycling.

4.2 Experimental Methods

Materials Synthesis: All chemicals are used as purchased without further purification. Li_2ZrCl_4 (LZC) solid electrolyte is synthesized by ball milling stoichiometric amounts of LiCl

(Sigma Aldrich, 99%) and $ZrCl_4$ (Sigma Aldrich, 99%) in sealed ZrO_2 jars for ten hours at 600 rpm (ref). LPSCl is purchased from supplier. $FeCl_3$ and FeF_3 composite cathodes are synthesized by ball milling FeCl3 (Sigma Aldrich 98%) and FeF_3 with the as-prepared Li_2ZrCl_4 and VGCF in a 50:50:4 wt ratio for six hours with a ball to material ratio of 60.

Materials Characterization: X-ray diffraction measurements are taken using a Bruker D2 Phaser with a Cu Kα source (λ = 1.54Å) from 28 to 58deg at a scan rate of 1deg/min. Samples are sealed in Kapton in an argon glovebox before being transferred to the XRD to prevent air exposure. *Electrochemical Characterization:* Impedance spectroscopy measurements are performed using a BioLogic potentiostat. All-solid-state cells are assembled using Swagelok cells. 150 mg of solid electrolyte was filled into a polyether ether ketone (PEEK) die with an inner diameter of 12.5 mm and pressed at 100 MPa for 2 min. On the anode side, 35 mg of LPSCl is deposited and again pressed at 100 MPa for 2 min. On the cathode side, 2 mg of cathode composite is uniformly distributed along with a thin piece of Ti foil (12.5mm diameter) to prevent potential corrosion of the pistons. The cell is then hard pressed at 350 MPa for 7 minutes. Lastly a 12.5mm diameter piece of In (Thermofisher) is placed on the LPSCl side along with a Cu-backed piece of Li (50um). The cell is then placed in an external steel frame applying a stack pressure of 45 MPa.

4.3 Results and Discussion

4.3.1 Redox potentials and hysteresis

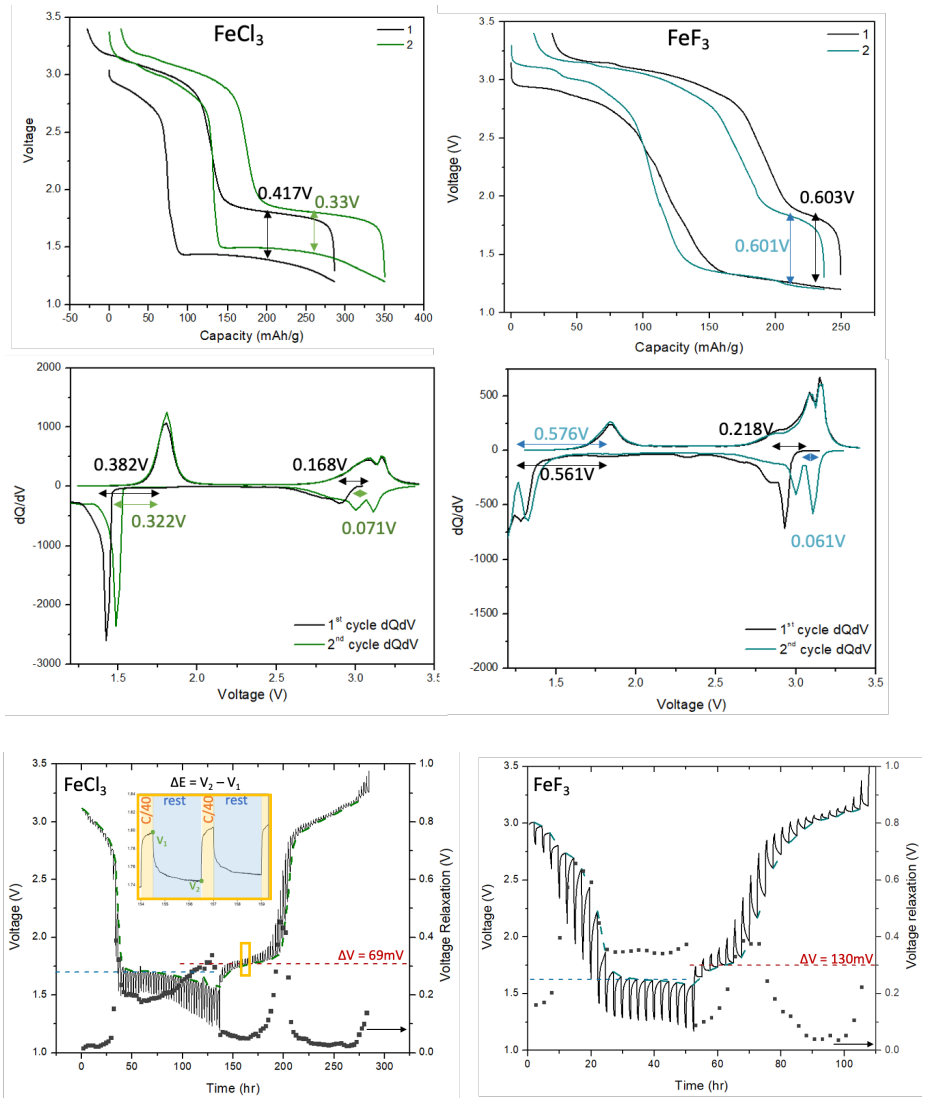

Figure 4.1: Charge and discharge curves for 1st and 2nd cycles of $FeCl_3$ (a) and FeF_3 (b) with corresponding dQ/dV plots (c, d). GITT measurements for the first cycles with plotted relaxation voltage and second plateau hysteresis data for $FeCl_3$ (e) and FeF_3 (f).

$FeCl_3$ and FeF_3 cells are cycled at C/20 to compare the performance of the second cycle and dQ/dV plots are analyzed to help show changes in peak shape (Figure 1 a-d). Minimal change in curve shape occurs between the first and second cycles, suggesting good stability and that there

is no significant change in reaction mechanism or side reactions (SI). Both $FeCl_3$ and FeF_3 have voltage plateaus at roughly 2.9V and 1.4V vs LiIn (3.5V and 2V vs Li) which match the general agreement in FeF_3 literature of an initial step to form Fe^{2+} and then further lithiation to Fe.

During the first cycle, $FeCl_3$ exhibits a lower hysteresis of around 400mV for the second plateau as compared to FeF_3 which experiences a ~600mV hysteresis. Interestingly, FeF_3 in a solid-state battery exhibits a significantly lower hysteresis than in liquid cells as previous literature reports a hysteresis of ~1V.[11]

While both cases exhibit lower than theoretical capacities, $FeCl_3$ achieves a higher capacity at around 280 mAh/g (compared to 496 mAh/g theoretical) and FeF_3 achieves around 250 mAh/g (compared to 711 mAh/g theoretical). A more complete reaction can be obtained by lowering the cut-off voltage, however that leads to electrolyte degradation. Meanwhile, the voltage plateaus are in good agreement with previous literature on the conversion of FeF_3 to FeF_2 to Fe.

GITT measurements are performed at a C/40 rate for 20 minutes, followed by a 2 hr rest for each point of open circuit (Figure 1 e-f). The voltage relaxation, measured by the difference in voltage between equilibrium potential at the end of rest and the potential at the end of discharge is plotted accordingly. During discharge, the voltage relaxation for the first plateau for both $FeCl_3$ and FeF3 is smaller than during the second plateau, reflecting a lower polarization for the insertion step of Fe^{3+} to Fe^{2+} than the subsequent conversion step of Fe^{2+} to Fe. $FeCl_3$ exhibits on average lower polarization than FeF_3 with voltage relaxation values of the first plateau at 27 mV and the second plateau at 206 mV while FeF_3 goes from 116 mV to 303 mV. This shows that the first lithiation step has overall less resistance in the chloride scenario than fluoride. Interestingly, during charging, the voltage relaxations during the first and second plateaus for both $FeCl_3$ and FeF_3 appear closer together, with the conversion step only slightly larger than the insertion step. This

may be due to the initial cost of the phase transformation of FeX_3 to LiX and Fe upon which subsequent reversal becomes easier.

4.3.2 Reaction kinetics probed by EIS

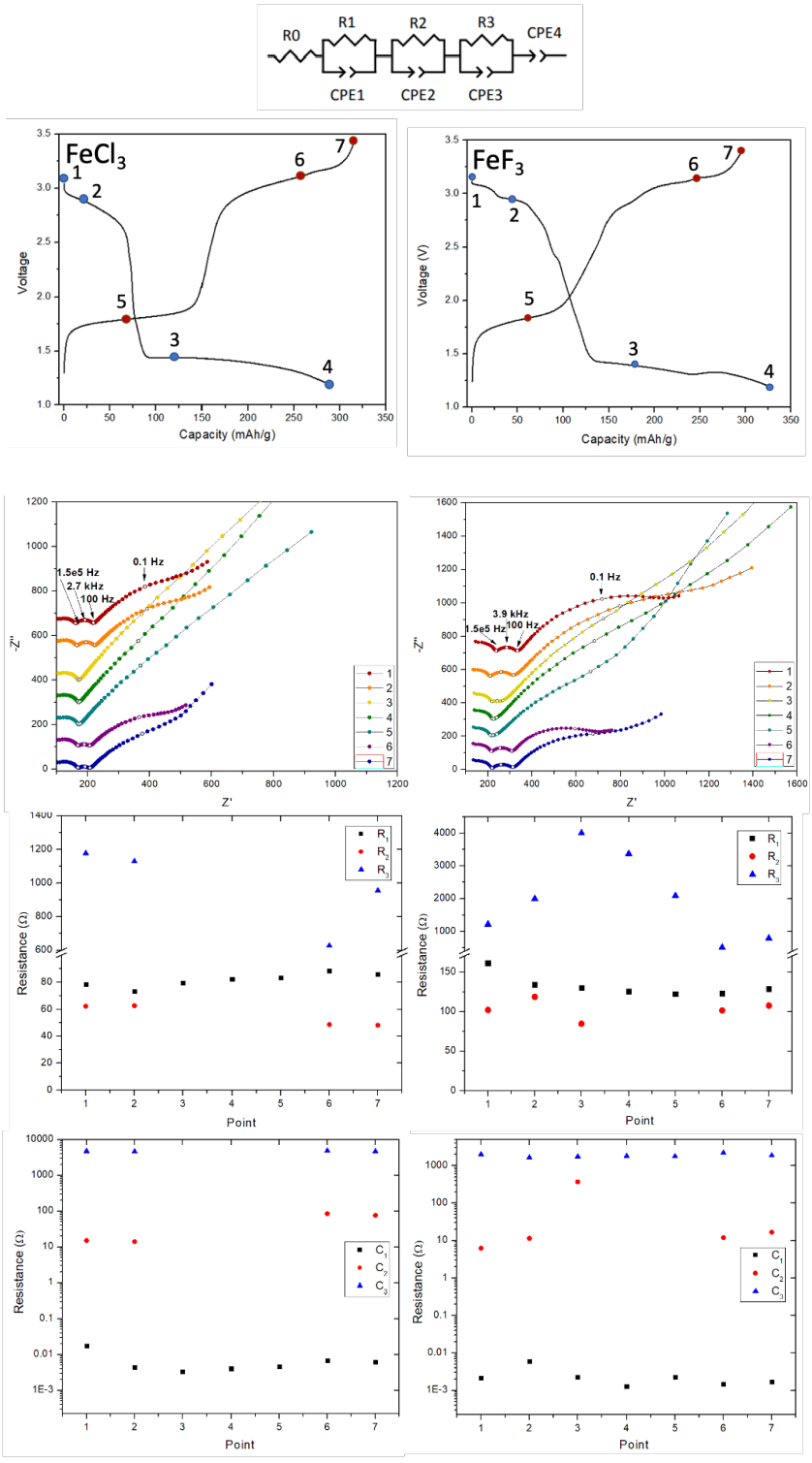

Figure 4.2: In-situ EIS of $FeCl_3$ (c) and FeF_3 (d) cells during various states of charge throughout the first cycle (a, b).

In order to better understand and compare the reaction kinetics, EIS measurements are taken at various states of charge during the first cycle (Figure 2). The cells are cycled at a C/20 rate and allowed to rest for 2 hrs to reach equilibrium before each measurement is taken. An equivalent circuit model of a resistor, three RC circuits and a constant phase element in series are used to fit the data. Four frequencies (150 kHz, 2.7 or 3.9 kHz, 100 Hz and 0.1Hz) are highlighted to help track the changes in impedance at different SOCs. In general, the impedance of the cell decreases during discharge and increases during charge, resulting in a very similar spectra after a full cycle and demonstrating the reversibility of the reaction.

The high frequency semicircle (~150 kHz) is attributed to the ionic resistance in the bulk and grain boundaries of the solid electrolyte (R_1) and understandably, stays relatively constant throughout charge and discharge for both $FeCl_3$ and FeF_3. The middle frequency semicircle, which is attributed to interfacial resistance at the LiIn interface (R_2), decreases during discharge and completely disappears in the $FeCl_3$ case by the end of discharge before reappearing during charge. In the FeF_3 case, the anode interface resistance appears to nearly disappear at the end of discharge but is still slightly present both before and after point 4. Lastly, the low frequency semicircle is attributed the charge transfer resistance (R_3) within the cathode. In the FeF_3 case, R3 exhibits the lowest resistance at the start and end of the cycle and a rapid increase in resistance during the middle portion between the second plateau on discharge and charge. This may reflect the rise in interfacial resistance between the new phases being formed as Fe^{2+} is reduced to Fe and then back to Fe^{2+} again. As the FeF_3 lithiates, there is not a significant change during the first plateau which is assumed to be an insertion mechanism, but rises during the conversion process in which nanoscale Fe precipitates out as Li continues to diffuse in to complete the formation of the two phase LiF/Fe nanocomposite.

4.3.3 Redox processes in $FeCl_3$ examined by XPS and XRD

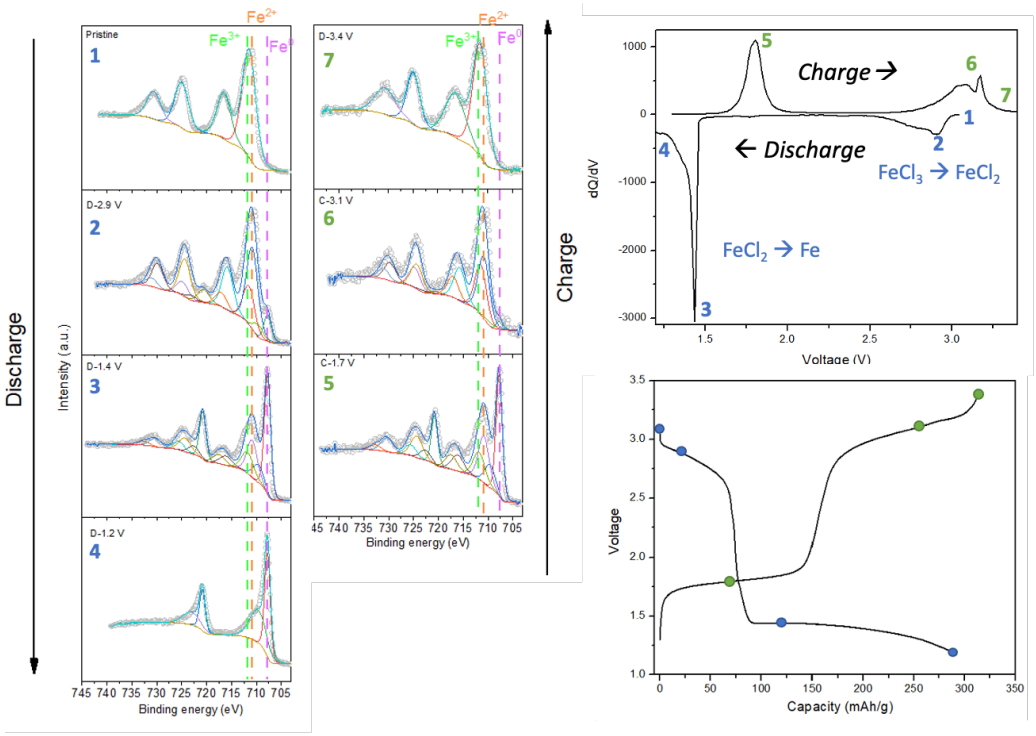

Figure 4.3: Ex-situ XPS of $FeCl_3$ cell during various states of charge throughout the first cycle.

To gain insight into the reaction mechanism, ex-situ XPS measurements were performed on disassembled $FeCl_3$ cells at varying states of charge throughout the first cycle (Figure 3). The cell was cycled at a C/20 rate and XPS measurements were taken of the pristine cell (1), after discharge at the first plateau and second plateaus (2, 3), end of discharge (4), charging back to second and first plateaus (5, 6) and fully charged (7). Specific voltages were determined through the dQ/dV plot. The pristine cell starts with a peak in binding energy correlating to Fe^{3+} at ~712 eV which begins to shift lower to 711 eV upon discharge at 2.9V showing the beginning of Fe2+ formation. Simultaneously a small Fe^0 peak at ~708 eV starts forming. This trend grows stronger upon further discharge to 1.4V where the main peaks are Fe^{2+} and Fe^0 and at full discharge, the main remaining peak is Fe^0 showing full conversion. The same trend is seen in reverse upon

charging as the Fe^{2+} peak reappears at 1.7V, starts shifting higher to the Fe^{3+} peak at 3.1V as the Fe^{0} disappears, and finally only the Fe^{3+} peak remains at full charge at 3.4V. The trends confirm the full reversibility of the reaction; however, they also speak to inhomogeneities as well. It appears the progression of Fe^{3+} to Fe^{2+} and Fe^{2+} to Fe^{0} experience overlap and may not be exclusively sequential reactions as Fe^{0} starts to show before full discharge occurs. Similar trends can be seen in work done on FeF_3 conversion batteries.

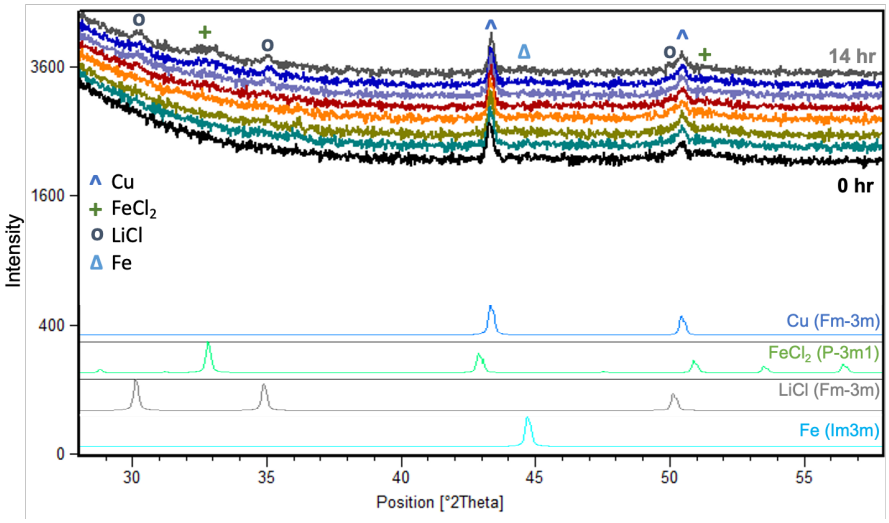

Figure 4.4: XRD of lithiation of $FeCl_3$ and KB powder over 14 hours, showing evolution of $FeCl_2$, LiCl, and Fe phases.

To complement the findings from XPS, XRD measurements are taken to better understand the reaction mechanisms that occur during discharge. To avoid the complications from the solid electrolyte, powders of $FeCl_3$ and FeF_3 mixed with Ketjen-black are ball milled and pressed onto a Li foil on an XRD holder and covered in Kapton tape to prevent air exposure. XRD measurements are then taken every two hours for 14 hours to detect changes and evolution in new phases. At the start, the only peaks present are from the Cu foil beneath the lithium; due to the ball milling, the $FeCl_3$ phase is amorphous with no sharp crystalline peaks, similar to the cathode

composite. As time progresses (~10hrs), LiCl and $FeCl_2$ peaks start to appear. By 14 hrs, there is also a small amorphous peak at 44.7deg corresponding to Fe.

4.3.4 Cycling performance

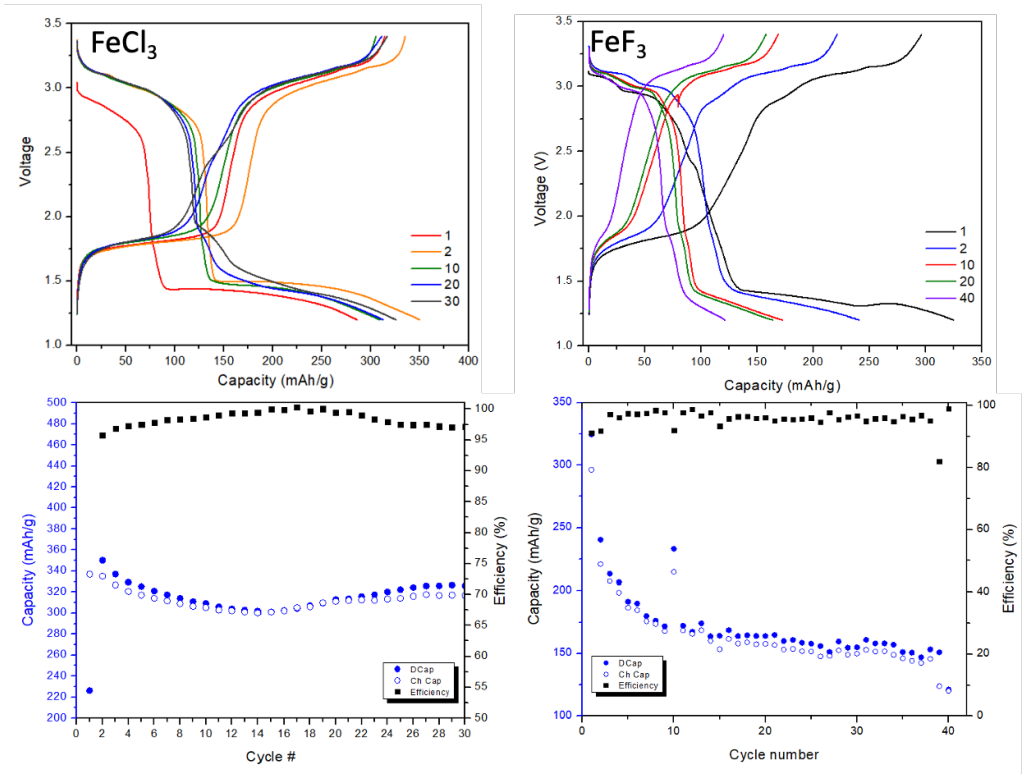

Figure 4.5: Cycling performance at a C/20 rate with charge/discharge curves and capacity retention and efficiencies are shown for $FeCl_3$ (a, c) and FeF_3 (b, d).

Lastly, the cycling performance of $FeCl_3$ and FeF_3 is compared at a C-rate of C/20 at room temperature. $FeCl_3$ shows stable cycling with good capacity retention and an average efficiency of ~98% for the first 30 cycles. FeF_3 shows a rapid capacity decay within the first ten cycles, after which the capacity appears to stabilize and the efficiency holds at ~96% for the first 30 cycles.

4.4 Conclusions

In conclusion, our work has shown the feasibility of a novel $FeCl_3$ conversion cathode for use in solid state batteries with good cycling performance and lower hysteresis than a traditional FeF_3 cathode.

There is room for future work to expand and improve the performance of $FeCl_3$. Many advancements on FeF_3 cathodes have focused on reducing the cathode particle size and changing its shape to promote a more efficient reconversion process and a similar approach may also be fruitful for $FeCl_3$. Synthesis of nano-sized FeF_3, FeF_3 nanowires, FeF_3/C nanocomposites, and FeF_3-CNT nanocomposites for use as conversion cathodes in liquid cells have all proven to help stability and increase capacity retention during cycling. Additionally, the use of a more stable halide electrolyte may help expand the operating voltage window and allow for higher capacity cycling.

4.4 Acknowledgments

Chapter 4, in part is currently being prepared for submission for publication of the material, V. Petrova, J. Zhou, S. Wang, P. Liu. The dissertation author was the primary researcher and author of this material.

REFERENCES:

(1) Ozhabes, Y.; Gunceler, D.; Arias, T. A. Stability and Surface Diffusion at Lithium-Electrolyte Interphases with Connections to Dendrite Suppression. **2015**, 1–7.

(2) Doe, R. E.; Persson, K. A.; Meng, Y. S.; Ceder, G. First-Principles Investigation of the Li-Fe-F Phase Diagram and Equilibrium and Nonequilibrium Conversion Reactions of Iron Fluorides with Lithium. *Chem. Mater.* **2008**. https://doi.org/10.1021/cm801105p.

(3) Hua, X.; Eggeman, A. S.; Castillo-martínez, E.; Robert, R.; Geddes, H. S.; Lu, Z.; Pickard, C. J.; Meng, W.; Wiaderek, K. M.; Pereira, N.; Amatucci, G. G.; Midgley, P. A.; Chapman, K. W.; Steiner, U.; Goodwin, A. L.; Grey, C. P. Revisiting Metal Fluorides as Lithium-Ion Battery Cathodes. *Nat. Mater.* **2021**. https://doi.org/10.1038/s41563-020-00893-1.

(4) Yuan, Y.; Wu, F.; Bai, Y.; Li, Y.; Chen, G.; Wang, Z.; Wu, C. Regulating Li Deposition by Constructing LiF-Rich Host for Dendrite-Free Lithium Metal Anode. *Energy Storage Mater.* **2019**, *16* (June 2018), 411–418. https://doi.org/10.1016/j.ensm.2018.06.022.

(5) Li, S.; Fan, L.; Lu, Y. Rational Design of Robust-Flexible Protective Layer for Safe Lithium Metal Battery. *Energy Storage Mater.* **2019**, *18* (September 2018), 205–212. https://doi.org/10.1016/j.ensm.2018.09.015.

(6) Cui, C.; Zhang, R.; Fu, C.; Xiao, R.; Li, R.; Ma, Y.; Wang, J.; Gao, Y.; Yin, G.; Zuo, P. Stable Lithium Anode Enabled by Biphasic Hybrid SEI Layer toward High-Performance Lithium Metal Batteries. *Chem. Eng. J.* **2022**, *433* (P2), 133570. https://doi.org/10.1016/j.cej.2021.133570.

(7) Tan, L.; Chen, Q.; Chen, P.; Huang, X.; Li, L.; Zou, K.; Liu, D. Lithium Chloride Protective Layer for Stable Lithium Metal Anode via a Facile Surface Chemistry. *J. Electroanal. Chem.* **2023**, *928* (October 2022), 117063. https://doi.org/10.1016/j.jelechem.2022.117063.

(8) He, M.; Guo, R.; Hobold, G. M.; Gao, H.; Gallant, B. M. The Intrinsic Behavior of Lithium Fluoride in Solid Electrolyte Interphases on Lithium. *Proc. Natl. Acad. Sci. U. S. A.* **2020**, *117* (1), 73–79. https://doi.org/10.1073/pnas.1911017116.

(9) Bai, P.; Ji, X.; Zhang, J.; Zhang, W.; Hou, S.; Su, H.; Li, M.; Deng, T.; Cao, L.; Liu, S.; He, X.; Xu, Y.; Wang, C. Formation of LiF-Rich Cathode-Electrolyte Interphase by Electrolyte Reduction. *Angew. Chemie - Int. Ed.* **2022**, *61* (26). https://doi.org/10.1002/anie.202202731.

(10) Liang, X.; Pang, Q.; Kochetkov, I. R.; Sempere, M. S.; Huang, H.; Sun, X.; Nazar, L. F. A Facile Surface Chemistry Route to a Stabilized Lithium Metal Anode. *Nat. Energy* **2017**, *2* (July), 1–7. https://doi.org/10.1038/nenergy.2017.119.

(11) Liu, P.; Vajo, J. J.; Wang, J. S.; Li, W.; Liu, J. Thermodynamics and Kinetics of the Li/FeF 3 Reaction by Electrochemical Analysis. *J. Phys. Chem. C* **2012**. https://doi.org/10.1021/jp211927g.

CHAPTER 5: CONCLUSIONS

In conclusion, this work has focused on using conversion reactions as a platform to study reaction kinetics, nanomorphology and formation mechanisms. AC impedance was developed as a novel tool to characterize in-situ solid-state reactions based on conductivity evolution during the reaction. Particle size is found to have an effect on the reaction pathway, especially tuning $FeCl_2$ due to the low mobility of Fe. Conversion reactions based on diluted metal halides were also used to study how to tune nanomaterial morphology, resulting in the synthesis of 1D Co nanowires without the use of external stimuli. Lastly, conversion cathode materials were studied in solid state batteries to compare the effects of different surface energies on the path hysteresis during cycling.

In this work, conversion reactions served as a broad platform to study different fundamentals in materials science from reaction kinetics to thermodynamics to nucleation and growth and engineering applications. There are still many directions that each of these projects can be extended to in the future. Developing AC impedance as a characterization tool to detect onset of reaction and track reaction progress allows it to be applied to many other reactions that involve the formation of a conducting species. Examples of such reactions include Fe_2O_3-MoO_3 and ZnO-WO_3 metathesis reactions. It would be interesting to see the technique applied simultaneously with a secondary in-situ technique such as synchrotron XRD and analyze the data in real-time.

The conclusions from the work done on Co NWs can also lead to new synthesis pathways. While the conversion step was done in liquid in a bulk approach, experimental methods can be modified. For example, the conversion reaction can take place electrochemically in a battery through lithiation of the Suzuki phase precursor. This would be limited by the ion transport of Li into the nanocomposite and may yield new results. Alternatively, due to cobalt's magnetic

properties, alignment of the nanowires may be possible by introducing a strong magnetic field during the conversion reaction. This may aid in producing a more uniform product and possibly help make the process more efficient and scalable.

Lastly, there is a lot more work to be done on the topic of $FeCl_3$ conversion reactions in batteries. Since $FeCl_3$ is essentially rust, an incredibly abundant, safe, and cheap material, being able to achieve good performance with it can help foster in a greener battery manufacturing process. As this is the first time $FeCl_3$ has been studied, there is much optimization to be done to help mitigate the eventual hysteresis it shows. While there are many challenges to tackle, this speaks to the excitement of the field and how it continues to learn, grow and expand with every new experiment and data point.